

Needles in a haystack I: Pilot ALMA 2 mm follow-up of bright dusty star-forming galaxies as a redshift filter

OLIVIA R. COOPER,¹ CAITLIN M. CASEY,¹ JORGE A. ZAVALA,^{1,2} JACLYN B. CHAMPAGNE,¹ ELISABETE DA CUNHA,^{3,4,5} JEYHAN S. KARTALTEPE,⁶ ARIANNA S. LONG,⁷ JUSTIN S. SPILKER,^{1,8,*} AND JOHANNES STAGUHN^{9,10}

¹Department of Astronomy, The University of Texas at Austin, 2515 Speedway Boulevard Stop C1400, Austin, TX 78712, USA

²National Astronomical Observatory of Japan, 2-21-1 Osawa, Mitaka, Tokyo 181-8588, Japan

³International Centre for Radio Astronomy Research, University of Western Australia, 35 Stirling Hwy, Crawley, WA 6009, Australia

⁴Research School of Astronomy and Astrophysics, Australian National University, Canberra, ACT 2611, Australia

⁵ARC Centre of Excellence for All Sky Astrophysics in 3 Dimensions (ASTRO 3D)

⁶School of Physics and Astronomy, Rochester Institute of Technology, 84 Lomb Memorial Drive, Rochester, NY 14623, USA

⁷Department of Physics and Astronomy, University of California, Irvine, CA 92697, USA

⁸Department of Physics and Astronomy and George P. and Cynthia Woods Mitchell Institute for Fundamental Physics and Astronomy, Texas A&M University, 4242 TAMU, College Station, TX 77843-4242

⁹The Henry A. Rowland Department of Physics and Astronomy, Johns Hopkins University, 3400 North Charles Street, Baltimore, MD 21218, USA

¹⁰Observational Cosmology Lab, Code 665, NASA Goddard Space Flight Center, Greenbelt, MD 20771, USA

(Dated: October 18, 2021)

ABSTRACT

A complete census of dusty star-forming galaxies (DSFGs) at early epochs is necessary to constrain the obscured contribution to the cosmic star formation rate density, however DSFGs beyond $z \sim 4$ are both rare and hard to identify from photometric data alone due to degeneracies in submillimeter photometry with redshift. Here, we present a pilot study obtaining follow-up Atacama Large Millimeter Array (ALMA) 2 mm observations of a complete sample of 39 850 μm -bright dusty galaxies in the SSA22 field. Empirical modeling suggests 2 mm imaging of existing, bright samples of DSFGs selected at 850 μm -1 mm can quickly and easily separate DSFGs by redshift, isolating the “needle in a haystack” DSFGs that sit at $z > 4$ or beyond. With available redshift constraints, we find a positive correlation between redshift and 2 mm flux density. Specifically, our models suggest the addition of 2 mm to a moderately well-constrained IR SED will improve the accuracy of a millimeter-derived redshift from $\Delta z/(1+z) = 0.3$ to $\Delta z/(1+z) = 0.2$. Combining archival submillimeter imaging with our measured ALMA 2 mm photometry ($1\sigma \sim 0.08 \text{ mJy beam}^{-1}$ RMS), we characterize the galaxies’ IR SEDs and use them to constrain redshifts. Our IR SED characterizations provide evidence for relatively high ($\langle \beta \rangle = 2.4^{+0.4}_{-0.3}$) emissivity spectral indices in the sample. From millimeter photometric redshifts we identify 7/39 high- z candidates each with $> 50\%$ likelihood for $z > 4$, and demonstrate the utility of 2 mm imaging as a redshift filter for DSFGs. We measure that especially bright $S_{850\mu\text{m}} > 5.5 \text{ mJy}$ galaxies contribute $\sim 10\%$ to the cosmic-averaged CSFRD from $2 < z < 5$, confirming findings from previous work with similar samples.

1. INTRODUCTION

Characterizing the growth mechanisms and prevalence of the most extreme star-forming galaxies is crucial in order to understand the cosmic star formation rate density (CSFRD) across cosmic time, a primary goal in extragalactic astronomy (Madau & Dickinson 2014). The history of cosmic star formation measured at rest frame UV/optical wavelengths currently extends to $z \gtrsim 10$

due to the relative ease of identifying Lyman Break Galaxies (LBGs) in deep *Hubble Space Telescope* and *Spitzer Space Telescope* imaging (e.g. Ellis et al. 2013; Oesch et al. 2013; Bouwens et al. 2015; Finkelstein et al. 2015; Finkelstein 2016). However, measuring solely unobscured star formation by surveying optical and UV emission alone neglects a non-negligible amount of star formation activity in the Universe.

Dusty Star-Forming Galaxies (DSFGs) dominate cosmic star formation at its peak epoch (Casey, Narayanan, & Cooray 2014), with extreme star formation rates

* NHFP Hubble Fellow

(SFRs) $\gtrsim 100 \text{ M}_\odot \text{ yr}^{-1}$, stellar masses $\gtrsim 10^{10} \text{ M}_\odot$, and high gas mass fractions $\sim 40 - 80\%$ (Carilli & Walter 2013). While high SFRs imply the presence of young, massive UV-emitting stars, much of the UV and optical stellar emission is obscured and re-radiated at longer wavelengths in the (sub)millimeter by dust. Therefore, multi-wavelength observations are necessary to take a full census of both unobscured and obscured cosmic star formation.

Most DSFGs are discovered in wide-area observations using single dish far-infrared/millimeter instruments such as the Submillimeter Common-User Bolometer Array (SCUBA/SCUBA-2) on James Clerk Maxwell Telescope (JCMT; e.g. Smail et al. 1997; Hughes et al. 1998; Chapman et al. 2005; Koprowski et al. 2017; Simpson et al. 2019), *Herschel Space Observatory*¹ (Pilbratt et al. 2010), and the AzTEC instrument (Scott et al. 2008; Aretxaga et al. 2011); multi-wavelength follow up of ~ 100 s of survey-identified DSFGs reveals most sit between $1 < z < 3$ (Casey et al. 2012a; Magnelli et al. 2011, 2013; Gruppioni et al. 2013; Le Floc'h et al. 2005). While there exists a number of individually studied DSFGs at redshifts as high as $z \sim 5 - 7$ (e.g. Cooray et al. 2014; Strandet et al. 2017; Marrone et al. 2018; Zavala et al. 2018b; Casey et al. 2019; Reuter et al. 2020), such high- z DSFGs have proven difficult to identify. DSFGs beyond $z \sim 4$ are needles in a haystack in classical submillimeter flux limited surveys, which are dominated by DSFGs at $z \approx 1 - 3$, as they are both rare and hard to identify due to submillimeter photometry degeneracies with redshift. Often, their strongly negative k -correction is a benefit to their detection, as the flux density of DSFGs at $z > 1$ remains constant with increasing z for observed wavelengths longer than $\sim 850 \mu\text{m}$, meaning a DSFG at $z \sim 10$ can be observed as readily as a DSFG at $z \sim 1$ (Blain et al. 2002). However, when searching for high- z DSFGs, this negative k -correction is also a hindrance as it becomes difficult to identify redshifts for galaxies with only long-wavelength emission. Their negative k -correction combined with (sub)millimeter color degeneracy between dust temperature and approximate redshift makes it easy to confuse $z \sim 2$ and $z \sim 6$ DSFGs barring clear identification at other wavelengths.

Previous samples at $z > 3$ lacked the completeness necessary to resolve whether high- z DSFGs play a significant role in cosmic star formation (e.g. Zavala et al. 2018a), distinguish between dust rich and dust poor

models of the cosmic SFH, and to constrain the high- z DSFG number density (Casey et al. 2018a,b). For example, Koprowski et al. (2017), Rowan-Robinson et al. (2016), Dudzevičiūtė et al. (2020), and Gruppioni et al. (2020) all present very different conclusions on the number density of IR luminous galaxies in the CSFRD at $z > 3$, due to either limited sample sizes at high redshift or fundamental differences in survey strategy. The recent Mapping Obscuration to Reionization with ALMA (MORA) survey (Zavala et al. 2021) used measurements of 2 mm number counts in a blank-field survey to make significant progress in constraining the dust-obscured contribution to the total CSFRD. They find the CSFRD contribution to be $\sim 35\%$ at $z = 5$ and only $20 - 25\%$ at $z = 6 - 7$, suggesting dust-obscured star formation plays a minor role in total star formation at early epochs. On the other hand, Gruppioni et al. (2020) find a flatter IRLF slope from $4.5 < z < 6$, with a significant contribution to the CSFRD from obscured sources at high redshift, though again, using a very different survey strategy. While studies like Zavala et al. (2021) and Gruppioni et al. (2020) provide a good benchmark for the contributions of obscured and unobscured sources to the CSFRD, large uncertainties remain, necessitating a complete census of DSFGs at early epochs.

Empirical modeling by Casey et al. (2018a,b) derived from simulated DSFGs emphasizes the value of longer wavelength observations for easily and cheaply selecting for high- z candidates. DSFGs selected at $850/870 \mu\text{m}$ with single wavelength measurements can be sorted roughly by redshift with interferometric 2 mm follow up imaging while simultaneously providing precise positions for these galaxies (e.g. da Cunha et al. 2021) given the improvement in resolution using an interferometer versus single-dish instruments. Staguhn et al. (2014) report the first deep GISMO 2 mm observations, and detect 15 sources in the Hubble Deep Field with a median redshift of $z = 2.9 \pm 0.9$, higher than the average redshift of $850 \mu\text{m}$ -selected DSFGs (e.g. Chapman et al. 2005). Magnelli et al. (2019) present deep GISMO 2 mm observations in COSMOS and find four $z > 3$ DSFGs of the five sources with (sub)millimeter counterparts in COSMOS catalogs, and suggest 2 mm surveys favor detection of massive, extremely star-forming, high- z galaxies. The MORA survey — the largest ALMA 2 mm blank-field contiguous survey (184 arcmin^2) — demonstrates this, finding an average redshift $\langle z \rangle = 3.5_{-0.2}^{+0.3}$, with 77% of sources at $z > 3$ and 30% at $z > 4$, effectively filtering out lower redshift DSFGs (Casey et al. 2021). Other millimeter wavelengths have been leveraged to select for higher redshift sources; for example, Zavala et al. (2018a) conduct a blind search at 3 mm and detect 16

¹ *Herschel* is an ESA space observatory with science instruments provided by European-led Principal Investigator consortia and with important participation from NASA.

sources at $> 5\sigma$, and Williams et al. (2019) serendipitously discover a $z \sim 5 - 6$ source at 3 mm. Reuter et al. (2020) find $\langle z \rangle = 3.9$ for a sample of gravitationally-lensed DSFGs selected at 1.4 mm, where the lensing and millimeter selections combine to filter out low-redshift sources.

In this paper, we present ALMA 2 mm observations of bright sources ($S_{850\mu\text{m}} > 5 \text{ mJy}$) identified with SCUBA-2 at $> 5\sigma$. Our goals are to identify the highest- z sources for further follow-up, provide an independent measurement of the volume density of $z > 3$ DSFGs, and test the practical utility of 2 mm follow up observations as a redshift filter for larger DSFG surveys. We describe the sample and observations in §2, and in §3 we present analysis of sources’ redshift and physical characteristics. §4 discusses the implications of our measurements, and §5 summarizes. We assume a Chabrier IMF (Kroupa 2001) and *Planck* cosmology throughout this paper, adopting $H_0 = 67.7 \text{ km s}^{-1} \text{ Mpc}^{-1}$ and $\Omega_\lambda = 0.6911$ (Planck Collaboration et al. 2016).

2. SAMPLE & OBSERVATIONS

2.1. Sample of DSFGs

In this project, we set out to measure 2 mm flux densities for a sample of bright 850 μm -selected DSFGs. To select our sample, we drew from the 850 μm -selected submillimeter galaxies (SMGs) observed with SCUBA-2 as part of the SCUBA-2 Cosmology Legacy Survey (S2CLS; Geach et al. 2017). S2CLS, initially conducted starting in 2011 on the James Clark Maxwell Telescope (JCMT), surveyed ~ 5 square degrees of sky at 850 μm . The largest and deepest survey of SMGs, the wide survey component of S2CLS includes seven extragalactic fields (UKIDSS-UDS, COSMOS, *Akari*-NEP, Extended Groth Strip, Lockman Hole North, SSA22, and GOODS-North) and reports 2851 submillimeter sources at 850 μm with a $\geq 3.5\sigma$ detection, with 1313 of those sources at $S_{\text{obs}} > 5 \text{ mJy}$. Over 90% of the total survey area reaches a sensitivity of below 2 mJy beam $^{-1}$, with a median depth per field of $\sim 1.2 \text{ mJy beam}^{-1}$ (Geach et al. 2017). The S2CLS survey is ongoing; see additional deep imaging in COSMOS presented in Simpson et al. (2019).

Our targets were first selected to lie in ALMA-accessible fields (COSMOS, UDS, and SSA22), and second, detected at $S_{850\mu\text{m}} > 5 \text{ mJy}$ with $> 5\sigma$ significance. We selected the brightest 850 μm -selected DSFGs for 2 mm follow up due to the observation that brighter DSFGs have a higher average redshift than galaxies at fainter submillimeter flux densities (Béthermin et al. 2015; Casey et al. 2018a,b). This paper presents a complete sample of 39 such bright DSFGs in SSA22 only;

given the depth of SCUBA-2 observations, the $> 5\sigma$ threshold translates to an effective flux density cut of $S_{850\mu\text{m}} > 5.55 \text{ mJy}$ in SSA22 given the $\sim 1.2 \text{ mJy RMS}$. The remaining targets in COSMOS and UDS are approved for observations in ALMA Cycle 8 and will be presented in a future work. Though the SSA22 subsample constitutes $\sim 9\%$ of the full sample to be observed, the subsample is sufficiently large to draw some conclusions on the nature of the brightest $\gtrsim 5 \text{ mJy}$ DSFGs.

2.2. ALMA Observations

ALMA observations of our sample in SSA22 were taken on 8 January 2020 as one target field of Project #2019.1.00313.S (PI: Casey). In this field, 39 individual targets were observed with ALMA’s Band 4 centered at 2 mm. ALMA pointings were centered on the reported S2CLS 850 μm positions (Geach et al. 2017). Each target was observed for ~ 1 min using the 12-m array, with angular resolution 1''.2 and local oscillator tuning 145 GHz. The observations had a PWV of 2.05 mm, with 43 antennae and total on-source time of 34.12 min (< 1 min per source). The phase calibrator was J2217+0220 and the bandpass calibration was J2253+1608. The baseline limit with good phase (80%) was 279 m (roughly a C43-2 configuration).

The ALMA images were reduced using the Common Astronomy Software Application (**CASA**) version 5.6.0². We adopted robust = 2 natural weighting to optimize imaging depth given the sources were unresolved at this resolution. The images were primary beam corrected, accounting for the primary beam response decreasing radially outwards from the center of the field. We derive flux density and noise measurements from primary-beam-corrected images using the **CASA** task `imstat`. The median RMS achieved was 0.08 mJy beam $^{-1}$ (range [0.07 – 0.11] mJy beam $^{-1}$), better than the requested RMS of 0.1 mJy. The synthesized beam for these observations is $1''.7 \times 1''.4$. On these scales ($\sim 12 \times 14.5 \text{ kpc}$ at $z = 2$), it is expected that all detected sources are unresolved, therefore we adopt the peak flux density from **CASA** `imstat` within the SCUBA-2 beam (7.5 arcsec radius) as the measured 2 mm flux density of the source. We confirmed the robustness of this method by comparing to measurements of the source flux using **CASA** `viewer` across an extended aperture, and found good agreement between the two measurement methods.

Given that all of our targets had prior SCUBA-2 detections, we invoked a 3σ detection threshold for our ALMA observations. While a 3σ detection threshold is

² <https://casa.nrao.edu>

below the nominal 5σ threshold for blank field detection, other works have demonstrated that prior-based measurements are far less burdened by contaminants (e.g. Hodge et al. 2013; Dunlop et al. 2017). Out of the 39 targets, 35 targets were detected in the 2 mm observations above this threshold. Only one detected target (SSA.0007) was resolved into two sources, and the remainder were singletons. The $850\mu\text{m}$ and 2 mm flux densities for all targets are listed in Table 1.

Comparing S2CLS reported coordinates to our measured coordinates of sources with flux densities $> 3\sigma$, we find an average RA offset of $1.^h64 \pm 0.^{\circ}92$ and an average Dec offset of $-1.^{\circ}0 \pm 0.^{\circ}7$, for a total net average offset of $1.^{\circ}9 \pm 1.^{\circ}2$. Some offset is expected, as SCUBA-2 is a single dish facility and achieves lower resolution and therefore lower astrometric precision than ALMA. We do find some systematic offset as illustrated by Figure 1, likely originating from the astrometric imprecision of SCUBA-2. Hodge et al. (2013) show a similar few arcsec systematic offset between LABOCA and ALMA detections for individual sources; similarly Simpson et al. (2015) find $\gtrsim 1''$ offsets between SCUBA-2 and ALMA detected sources.

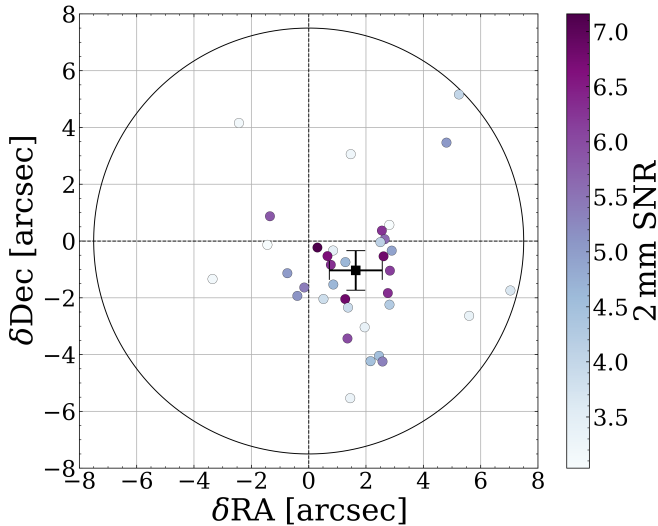


Figure 1: Positional offset between ALMA and SCUBA-2 centroids for the $S_{2\text{mm}} > 3\sigma$ sources in our sample, colored by single-to-noise ratio (SNR) in ALMA data centered on SCUBA-2 positions (pointing centers). The black square shows the average offset and uncertainties. While there is systematic offset between the SCUBA-2 and ALMA positions, nearly all detected sources lie well within the SCUBA-2 beam FWHM, represented by the black circle. Those far offset tend to have lower SNR suggesting a higher probability of chance alignment.

We adopt deboosted flux densities from S2CLS (Geach et al. 2017) to account for confusion and Eddington boosting. The median offset between deboosted and observed $S_{850\mu\text{m}}$ flux densities in our catalog is 0.8 mJy ($\lesssim 20\%$ of the total flux density), less than the reported uncertainty for each individual source’s flux density (which averages to 1.17 mJy).

2.3. The SSA22 Field

The SSA22 field was first observed as one of four small selected areas (SSA) chosen for deep multiband imaging followed by complete follow-up spectroscopy. The initial deep imaging was part of the Hawaii K-Band Galaxy Survey, and was first presented in Cowie et al. (1994), with follow-up spectroscopy detailed in Songaila et al. (1994) and Cowie et al. (1996).

The now well-known protocluster structure in SSA22 at $z = 3.09$ was first revealed by Steidel et al. (1998). Protoclusters are rich, overdense regions thought to be the progenitors of massive clusters in the local Universe (Overzier 2016). The SSA22 protocluster hosts intense star formation activity, and has an abundance of Lyman break galaxies (LBGs, e.g. Steidel et al. 1998), distant red galaxies (DRGs, e.g. Uchimoto et al. 2012), Lyman- α emitters (LAEs, e.g. Hayashino et al. 2004; Yamada et al. 2012), Lyman- α blobs (LABs, e.g. Steidel et al. 2000; Matsuda et al. 2004, 2011), and a rare overdensity of DSFGs (e.g. Stevens et al. 2003; Tamura et al. 2009; Geach et al. 2005; Umehata et al. 2015, 2017).

Several works have noted that DSFGs may act as signposts for overdense regions or protoclusters at high redshift (Casey 2016; Lewis et al. 2018), although Miller et al. (2015) claims that SMGs are poor tracers of protoclusters. Nevertheless, a number of DSFGs have been detected in the SSA22 field, originally discovered with SCUBA-2 observations (e.g. Chapman et al. 2001, 2004a). Additional SSA22 DSFGs have been detected in AzTEC or ALMA 1.1 mm maps (e.g. Tamura et al. 2009; Umehata et al. 2014, 2015, 2018), some of which have optical to near-infrared and/or millimeter to radio photometric redshifts consistent with the protocluster. Umehata et al. (2017, 2018) map a small central region (ADF22) of the protocluster with ALMA, revealing an unusually high number of DSFGs at the protocluster core, including intrinsically fainter DSFGs ($S_{1.1\text{mm}} < 1\text{mJy}$). While a few dozen DSFGs have been characterized in the central region of SSA22 (Umehata et al. 2018), about a third of which are spectroscopically confirmed in the protocluster, very few of those are $S_{850\mu\text{m}} > 5\text{mJy}$. Thus, those fainter DSFGs are excluded from the analysis in this paper.

While SSA22 is home to this well known protocluster structure and overabundance of DSFGs, we wish to highlight that the field's population of $S_{850\mu\text{m}} > 5.55 \text{ mJy}$ DSFGs are not overabundant or more common than the cosmic average based on measurements of bright $850\mu\text{m}$ number counts. In other words, there is no direct evidence for a statistical excess in the field due to the well-studied overdensity. We explore this further in §4.4.

2.4. Redshifts from the Literature

We crossmatch spectroscopic and photometric redshifts of galaxies in the SSA22 field to our sample. The target SSA.0001 is a confirmed protocluster member reported in Umehata et al. (2014) to have a spectroscopic redshift of $z = 3.092$. This source is the brightest AzTEC source ($S_{1.1\text{mm}} = 11.3 \pm 0.9 \text{ mJy}$) in Umehata et al. (2015). SSA.0007, resolved into two components in our 2 mm data, is also spectroscopically confirmed as part of a dense group within the protocluster at $z = 3.09$, possibly in a multiple merger phase (Umehata et al. 2015; Kubo et al. 2016; Umehata et al. 2017, 2018, 2019). In addition to the sources confirmed in the protocluster, three galaxies are confirmed spectroscopically to be in the foreground of the protocluster: SSA.0009 at $z = 2.555$ (Chapman et al. 2005), SSA.0019 at $z = 2.278$ (Alaghband-Zadeh et al. 2012), and SSA.0031 at $z = 2.6814$ (confirmed via Lyman- α emission; Cooper et al. in prep). About a third of our targets (14/39) also have OIR photometric redshifts and about one quarter (9/39) have mm/radio photometric redshifts (beyond those we calculate herein) reported in Umehata et al. (2014). In §3.1, we analyze protocluster membership for our sample relative to likely foreground and background sources.

2.5. Ancillary Data

We crossmatch our sample to the X-ray catalog for SSA22 presented in Lehmer et al. (2009) to check for the presence of luminous AGN. AGN could be a concern in using millimeter photometry to constrain redshifts, as AGN can heat ISM dust to temperatures warmer than galaxies without AGN. Fifteen sources have X-ray coverage but just two sources (SSA.0001 and SSA.0007) have significant X-ray detections ($0.5\text{--}8\text{ keV}$ luminosities within $10^{43} - 10^{45} \text{ erg s}^{-1}$) indicating AGN activity for those targets. This suggests the sample as a whole is not dominated by AGN, and that the presence of AGN is unlikely to impact the millimeter photometric analysis presented later in this paper as both SSA.0001 and SSA.0007 have secure spectroscopic redshifts.

We crossmatch our SSA22 sources with reported AzTEC 1.1 mm flux densities from Umehata et al.

(2014) and find $\sim 70\%$ (27/39) of our sample has reported 1.1 mm flux densities down to SNR of 3.8. This threshold corresponds to a flux density detection limit of $S_{1.1\text{mm}} \gtrsim 2.45\text{--}4.55 \text{ mJy beam}^{-1}$. Flux densities at 1.1 mm for the other 12 sources were extracted from the AzTEC map at the best available positions (precise ALMA 2 mm positions for 2 mm detections, else SCUBA-2 850 μm positions), with one source (SSA.0010) lying outside the AzTEC field.

Herschel/SPIRE measurements at 250 μm , 350 μm , and 500 μm of SSA22 were originally presented in Kato et al. (2016). A subset of sources has extracted flux densities using cross matches to positional priors from MIPS 24 μm , which were measured by Swinbank et al. (2014). Note that we do not use the MIPS 24 μm data directly because the depth varies significantly across the field and the coverage is incomplete. Furthermore, at the expected redshifts of our sources ($z \approx 2 - 6$), observed 24 μm does not probe rest-frame FIR emission, but instead measures the mid-IR, rich with complex Polycyclic Aromatic Hydrocarbon (PAH) emission and Silicon absorption that we are not attempting to constrain in this work. The SPIRE maps in Swinbank et al. (2014) are deblended by oversampling to 1''/pixel from the original *Herschel*/SPIRE 8'' pixel maps, and the extended cirrus emission from the Milky Way's interstellar medium is subtracted. About half of our sample (20/39) overlaps with the MIPS 24 μm coverage, and from this subset we identified 18/39 cross matches from the Swinbank et al. (2014) catalog within the MIPS 24 μm FWHM of 7''. For another 19 sources, we directly extract flux densities from deblended *Herschel*/SPIRE maps using our best positional constraints (Swinbank et al. 2014). The flux densities of the final two sources were extracted from the point source *Herschel*/SPIRE maps (optimized for point source extraction, ideal for our unresolved sources), as they lay outside the Swinbank et al. (2014) catalog and maps. We compared flux densities of overlapping sources from the point source *Herschel*/SPIRE maps and the deblended Swinbank et al. (2014) maps and catalog, and find no statistical differences within uncertainty. All of our measurements from the *Herschel* data are confusion limited (Nguyen et al. 2010).

For sources without positional priors in the Swinbank et al. (2014) catalogs (i.e. those with flux densities extracted from the deblended maps directly) we conduct a statistical analysis of cataloged sources from Swinbank et al. (2014) to infer an appropriate RMS for our *Herschel* flux density measurements. For each flux density measurement, we calculate the 68% confidence interval of the catalog RMS values within a 0.01 dex bin centered on the measured flux density. As the data are confusion

Name	R.A. hms	Dec. (J2000) dms	$S_{850\mu\text{m}}^{\text{deboost}}$ mJy beam $^{-1}$	$S_{2\text{mm}}$ mJy beam $^{-1}$
SSA.0001	22:17:32.41	+00:17:43.8	14.5±1.1	0.55±0.09
SSA.0002	22:16:55.62	+00:28:46.1	10.7±1.4	0.26±0.07
SSA.0003	22:16:59.83	+00:10:39.8	10.2±1.5	[0.2±0.07]
SSA.0004	22:16:51.24	+00:18:20.7	10.0±1.4	0.36±0.07
SSA.0005	22:17:18.79	+00:18:09.5	7.9±1.3	[0.23±0.08]
SSA.0006	22:18:06.61	+00:05:20.6	8.8±1.8	0.57±0.08
SSA.0007	22:17:37.02	+00:18:22.6	7.2±1.3	0.67±0.11
SSA.0007.1	22:17:37.02	+00:18:22.6	7.2±1.3†	0.34±0.08
SSA.0007.2	22:17:36.98	+00:18:20.61	7.2±1.3†	0.33±0.08
SSA.0008	22:18:06.46	+00:11:34.5	7.7±1.5	0.21±0.07
SSA.0009	22:17:33.93	+00:13:52.0	7.34±1.09	0.47±0.07
SSA.0010	22:17:01.11	+00:33:31.4	8.9±2.0	0.49±0.08
SSA.0011	22:18:27.88	+00:25:36.4	7.1±1.5	0.53±0.08
SSA.0012	22:17:43.24	+00:12:31.9	7.0±1.4	0.33±0.07
SSA.0013	22:16:57.31	+00:19:24.0	6.9±1.5	0.4±0.07
SSA.0014	22:18:15.26	+00:19:56.9	7.3±1.4	0.59±0.09
SSA.0015	22:16:52.19	+00:13:42.3	6.8±1.5	0.44±0.08
SSA.0016	22:18:06.19	+00:04:01.5	8.7±2.0	0.44±0.07
SSA.0017	22:17:44.04	+00:08:21.8	6.5±1.5	0.21±0.07
SSA.0018	22:17:28.31	+00:20:26.2	6.3±1.3	0.52±0.08
SSA.0019	22:17:42.26	+00:17:02.3	6.0±1.4	0.36±0.07
SSA.0020	22:18:27.20	+00:19:31.3	5.6±1.5	0.25±0.08
SSA.0021	22:17:41.35	+00:26:41.5	5.8±1.4	0.36±0.07
SSA.0022	22:18:23.61	+00:26:33.1	6.0±1.4	0.38±0.08
SSA.0023	22:18:17.21	+00:29:32.7	5.8±1.3	0.31±0.08
SSA.0024	22:18:10.12	+00:15:55.2	5.7±1.4	[0.18±0.07]
SSA.0025	22:17:09.51	+00:14:08.9	5.5±1.5	0.38±0.08
SSA.0026	22:18:13.51	+00:20:31.2	5.5±1.3	0.59±0.09
SSA.0027	22:16:32.20	+00:17:46.4	5.6±1.4	0.39±0.09
SSA.0028	22:16:50.06	+00:22:48.4	5.3±1.3	0.35±0.08
SSA.0029	22:18:27.10	+00:21:36.4	5.13±1.25	0.28±0.07
SSA.0030	22:18:33.06	+00:18:42.2	5.41±1.23	0.24±0.08
SSA.0031	22:17:17.43	+00:31:37.4	5.1±1.4	0.26±0.08
SSA.0032	22:17:32.31	+00:29:30.7	5.1±1.3	0.27±0.08
SSA.0033	22:17:03.52	+00:26:03.7	4.9±1.3	0.25±0.08
SSA.0034	22:17:02.27	+00:15:53.9	4.9±1.3	0.23±0.07
SSA.0035	22:18:06.72	+00:06:30.9	5.6±1.4	0.65±0.10
SSA.0036	22:17:31.78	+00:14:54.5	4.9±1.3	[0.20±0.07]
SSA.0037	22:18:29.06	+00:08:35.0	6.3±1.9	0.25±0.07
SSA.0038	22:17:02.95	+00:24:39.2	4.8±1.3	0.29±0.07
SSA.0041	22:18:34.99	+00:21:42.6	6.0±1.3	0.45±0.08

Table 1: All SSA22 targets observed in Band 4 with ALMA. Positions are in J2000, with 2 mm detected source positions from CASA `imstat` measurements. $S_{850\mu\text{m}}^{\text{deboost}}$ is the 850 μm flux density in mJy beam $^{-1}$ reported from S2CLS (Geach et al. 2017) and $S_{2\text{mm}}$ is our measured 2 mm flux density in mJy beam $^{-1}$. All sources with $\text{S/N} > 3$ from ALMA are considered detections given the SCUBA-2 detection as a prior; flux densities of non-detections at 2 mm are listed in brackets. †Reported flux density here is the sum of the two components as it is unresolved with this instrument.

limited, we adopt the confusion error from Nguyen et al. (2010) for any sources with derived errors less than these confusion error limits. This is a conservative estimate of the noise given the uncertainty in positional priors of deblended catalogs; in other words, at or below the confusion limit, confidence in the accuracy of positional priors is greatly reduced.

For our photometric redshift and SED fitting, we add absolute flux scale calibration uncertainty in quadrature with the statistical photometric uncertainties, taking that calibration error to be 4% for *Herschel* (Bendo et al. 2013), 5% for SCUBA-2 (Simpson et al. 2020), 10% for AzTEC (Wilson et al. 2008), and 5% for ALMA (Braatz 2021).

3. REDSHIFT AND FIR SED ANALYSIS

We characterize the sample of galaxies by their FIR/mm photometry to identify the highest redshift candidates and use the new 2 mm data to help constrain dust SEDs for our targets.

3.1. Photometric Redshifts

We derive a millimeter-based photometric redshift using the **MMpz** tool for each galaxy in our sample, as detailed in Casey (2020). **MMpz** uses rest-frame FIR/mm reprocessed dust emission to derive a photo- z probability density distribution based on the observed distribution of galaxy SEDs in the empirical relation between rest-frame peak wavelength and total IR luminosity, the $L_{\text{IR}}-\lambda_{\text{peak}}$ plane. The technique accounts for intrinsic SED breadth due to a range of dust temperatures at fixed IR luminosity. Estimating redshifts in the long wavelength photometric regime suffers from a strong degeneracy of millimeter flux density and colors with redshift; this algorithm is suited for data like these that lack other redshift constraints from spectroscopy or OIR photometry. Further, here we target a bright subset of DSFGs, a regime where OIR photo- z estimates can often be less accurate given differential attenuation with wavelength due to complex geometries (Casey et al. 2012b; da Cunha et al. 2015). Note that **MMpz** assumes the dust emissivity spectral index $\beta = 1.8$, which is a parameter fit during the dust SED characterization described in §3.2. Fixing β in this way has a minimal impact for use in photometric redshift fitting given the large uncertainties on redshift constraints from temperature degeneracies; see Casey (2020) for further discussion.

Comparing **MMpz** photo- z results to 12 OIR photo- z 's from Umehata et al. (2014), we calculate $\Delta z/(1+z) = 0.13$ with no systematic offset. Note that our comparison to OIR photo- z 's excludes SSA.0028, which has a reported OIR photo- z of $z = 0$, inconsistent with both

our FIR results and publicly available shallow SDSS optical imaging, which shows no obvious local universe source within $0.2'$ (Ahumada et al. 2020). Additionally, we exclude source SSA.0006 which has an OIR photo- z of $z = 6$; its detection at $24 \mu\text{m}$ likely precludes such a high redshift solution. While the sample of galaxies with existing spectroscopic redshifts is much smaller (limited to SSA.0001, SSA.0007, SSA.0009, SSA.0019, and SSA.0031), we find good agreement of $\Delta z/(1+z) = 0.04$ between our **MMpz** results and spectroscopic redshifts.

In order to characterize bulk properties of these galaxies in the absence of precise redshift information, we use **MMpz** photo- z probability density distributions to sort the sample into three redshift bins, with the middle bin at $2.6 < z < 3.6$, centered on the SSA22 protocluster redshift of $z = 3.1$. Note that while we use a protocluster category to sort the sample into redshift bins, we set a bin size much larger than the spectroscopically confirmed protocluster redshift range as we do not expect the presence of the protocluster to bias our sample; we quantify this further in Section §4.4. To bin the sample, we integrate the PDF in each interval of width $\Delta z = 0.1$ and consider the 3 highest probability redshift intervals. If any of the redshift bins with highest probability are within $\Delta z = 0.5$ of $z_{\text{SSA22}} = 3.1$, the galaxy is categorized in the protocluster bin. If the highest probability redshift intervals are lower or higher than the protocluster, they are binned as low- z or high- z , respectively. In a couple of cases, the 3 highest probability redshift intervals span multiple bins, with only one in the protocluster bin (e.g. protocluster and low- z , or protocluster and high- z). In these cases we categorize the galaxy in the protocluster bin. This binning technique accounts for the width of the photo- z PDF, rather than only considering the PDF peak. This results in low- z -binned sources ranging $1.2 < z < 2.4$, protocluster-binned sources ranging $2.5 < z < 3.6$, and high- z -binned sources ranging $3.4 < z < 4.7$.

From our millimeter photo- z measurements, we find 15 low- z galaxies with median $\langle z_{\text{low-}z} \rangle = 2.03 \pm 0.13$, 17 candidate protocluster members with median $\langle z_{\text{protocluster}} \rangle = 2.98 \pm 0.17$, and 7 high- z galaxies with median $\langle z_{\text{high-}z} \rangle = 3.83 \pm 0.16$, as shown in Figure 2. For the full sample, we find a median $\langle z \rangle = 2.6 \pm 0.2$. Errors on the median redshifts are derived from bootstrapping.

Note that **MMpz** takes both color and luminosity into account, and presumes no redshift evolution of λ_{peak} (and therefore, T_{dust}). Therefore, we expect z_{MMpz} to have some correlation with 2 mm flux density. This correlation, as well as the utility of 2 mm flux densities as a redshift filter, is discussed further in §4.2.

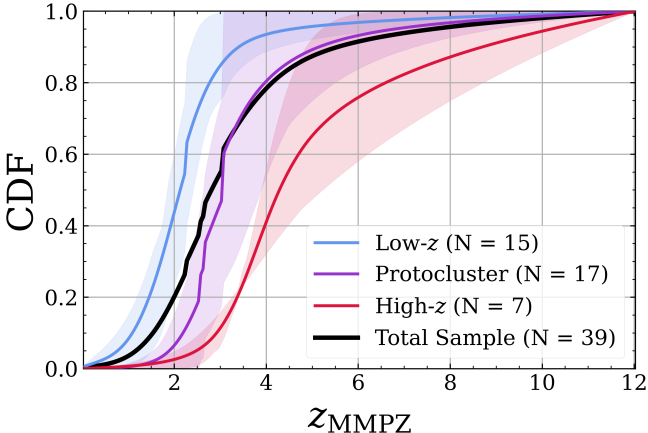


Figure 2: Redshift cumulative probability distribution functions (CDFs) from **MMpz**, with any spectroscopic redshift represented as delta functions at the measured redshift. The full sample is shown in black, and in blue, purple, and red are the CDFs for the low redshift, protocluster, and high redshift bins, respectively. The shaded regions show the 68% confidence interval for each redshift bin based on the individual **MMpz** fits. For the high- z sample, $\sim 60\%$ of the aggregate probability distribution is at $z > 4$.

3.2. IR SED Characterization

Though most galaxies in the sample lack precise redshift constraints, we fit available data using redshift constraints we have to infer basic characteristics about the galaxies' SEDs. For sources lacking spectroscopic redshifts, we use photometry to derive a redshift from **MMpz**, then fix that redshift solution in our SED fitting routine to the photometry. Note this degeneracy limits the scope of our conclusions as it may lead to underestimated uncertainties. Since the new 2 mm data is on the Rayleigh-Jeans tail, we focus our analysis on that portion of the spectrum.

Each galaxy's FIR/mm SED is fit to a modified blackbody added piecewise with a mid-infrared power law. We utilize a technique similar to that described in [Casey \(2012\)](#), but replace least-squares fitting with Bayesian analysis; the full tool will be presented in a forthcoming publication (Drew et al. in prep.). The mid-infrared power law is joined to the modified blackbody at the point where the blackbody slope is equal to the power law index $\alpha_{\text{MIR}} = 2$ (consistent with other works, e.g. [Kovács et al. 2010](#); [Casey 2012](#); [U et al. 2012](#)). The general opacity model is assumed, where $\tau = 1$ at $\lambda_{\text{rest}} = 200 \mu\text{m}$ (e.g. [Conley et al. 2011](#); [Greve et al. 2012](#)). Best fit SEDs are found based on a Markov Chain Monte Carlo convergence.

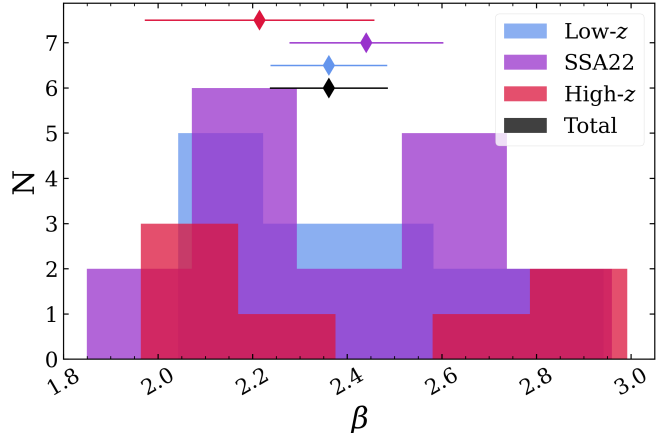


Figure 3: A histogram of measured emissivity spectral index (β) grouped by redshift bin. Low redshift sources are shown in blue, sources within the protocluster redshift in purple, and high redshift sources in red. The median β with uncertainty is plotted above the histogram for each redshift bin. All three distributions are consistent within error with median $\beta = 2.4 \pm 0.3$.

Input into the IR SED fitting routine is the best available redshift prior (fixed to the z_{MMpz} solution or $\text{spec-}z$ if available) and the FIR/mm photometry (at $250 \mu\text{m}$, $350 \mu\text{m}$, $500 \mu\text{m}$, $850 \mu\text{m}$, $1100 \mu\text{m}$, and $2000 \mu\text{m}$) with associated uncertainties. Our fixed parameters are $\alpha_{\text{MIR}} = 2$ and $\lambda_0 = 200 \mu\text{m}$, near the intrinsic peak of the dust SED. As neither can be directly constrained in this dataset, these broad population averaged values are assumed. We do include a CMB correction term in our fitting procedure to account for ISM dust heating from the CMB at high redshift ([da Cunha et al. 2013](#)), however, since the galaxies in our sample are predominantly at $z < 5$, this CMB correction is quite small for our sample in practice.

We used the SED fitting algorithm to find the best fit SED with measurements for each free parameter: emissivity spectral index (β), total infrared luminosity (L_{IR} , taken from 8–1000 μm), dust temperature (T_{dust}), and rest-frame peak wavelength (λ_{peak}). The last two variables have a fixed relationship given our assumed opacity model with $\lambda_0 = 200 \mu\text{m}$ (see Figure 20 of [Casey, Narayanan, & Cooray 2014](#)).

Overall, our median sample properties are comparable to other samples of DSFGs. As our targets are selected for being among the brightest 850 μm -selected DSFGs in the SCUBA-2 survey, we find generally high IR luminosities such that all may be categorized as ultraluminous IR galaxies (ULIRGs), with a median and standard deviation of $\log L_{\text{IR}} = 12.66 \pm 0.16 L_{\odot}$. Our sample is comparable to other samples with IR luminosities a few

times $10^{12} L_{\odot}$ (Dudzevičiūtė et al. 2020; da Cunha et al. 2015; Miettinen et al. 2017).

We convert our L_{IR} measurements to a SFR using the TIR calibrator from Hao et al. (2011) and Murphy et al. (2011), consistent with the review Kennicutt & Evans (2012). We find characteristically high SFRs $\sim 500 - 1000 M_{\odot} \text{ yr}^{-1}$, with median SFR = $690 \pm 270 M_{\odot} \text{ yr}^{-1}$. While this is somewhat higher than other studies, with a median SFR of $290 M_{\odot} \text{ yr}^{-1}$ found for the Dudzevičiūtė et al. (2020) sample, and $280 M_{\odot} \text{ yr}^{-1}$ in da Cunha et al. (2015), we expect higher SFRs corresponding to our bright $S_{850 \mu\text{m}} > 5.55 \text{ mJy}$ sample selection (the effective flux density cut given our criteria of $S_{850 \mu\text{m}} > 5.5 \text{ mJy}$ detection at $> 5\sigma$ in SSA22 given the $\sim 1.2 \text{ mJy RMS}$).

Peak wavelength measurements span $92 \mu\text{m} < \lambda_{\text{peak}} < 128 \mu\text{m}$, and consequently dust temperatures span $36 \text{ K} < T_{\text{dust}} < 53 \text{ K}$, with a median $T_{\text{dust}} = 44 \pm 4 \text{ K}$. Dudzevičiūtė et al. (2020) find a slightly lower median dust temperature of 30.4 K for their sample, with no evolution in T_{dust} at constant IR luminosity from $1.5 < z < 4$. da Cunha et al. (2021) also find a median $T_{\text{dust}} = 30_{-8}^{+14} \text{ K}$. We note that T_{dust} is not consistently defined and relies on assumptions of β and $\lambda = 0$, which are degenerate with T_{dust} (e.g. Figure 6 in Spilker et al. 2016). Further, da Cunha et al. (2021) find that optically-thin models tend to bias the temperature low compared with optically thick models.

Though our sample is $850 \mu\text{m}$ selected, and thus prone to bias towards intrinsically colder systems at $z \sim 2$ (Eales et al. 2000; Chapman et al. 2004b; Casey et al. 2009), our selection of brighter targets at higher L_{IR} is expected to correlate to hotter dust temperatures. Lee et al. (2013) use *Herschel*, which is unbiased at $z \sim 2$ with respect to dust temperature, and show that there are not many hot dust sources to be found unless they have luminous AGN. Therefore, our dataset represents a good sampling of galaxies above characteristic luminosity $L_{\text{IR}} > 3 \times 10^{12} L_{\odot}$ at the $S_{850 \mu\text{m}} > 5.55 \text{ mJy}$ flux density limit; though there exists a bias with respect to dust temperature for this study, we don't expect many intrinsically hotter sources.

Overall, the measured emissivity spectral index, β , is consistent (within uncertainties) for the three subsamples at $\beta \sim 2.4$, with a median and standard deviation of $\langle \beta \rangle = 2.4 \pm 0.3$ for the full sample. The median value for the low- z bin is $\langle \beta_{\text{low-}z} \rangle = 2.36 \pm 0.13$, for the protocluster bin is $\langle \beta_{\text{protocluster}} \rangle = 2.44 \pm 0.17$, and for the high- z bin is $\langle \beta_{\text{high-}z} \rangle = 2.2 \pm 0.3$ (see Figure 3). Errors on the medians are derived from bootstrapping. The use of ALMA data with single-dish SCUBA-2 data, possibly suffering from confusion boosting, could impact individ-

ual derivations of β in this sample. Though we have accounted for deboosting as best as possible, the precision to which any individual β can be measured can only be improved with matched-beam ALMA data at both frequencies.

Using our 2 mm dust continuum emission, we derive a gas mass for each galaxy by Equation 16 in the Appendix of Scoville et al. (2016). We adopt a single mass-weighted dust temperature of 25 K (consistent with Scoville et al. 2016; Casey et al. 2019) for this calculation rather than our SED measurements of T_{dust} , which are luminosity-weighted. Our gas mass estimates show most of our targets are gas-rich with $M_{\text{gas}} \sim 10^{11} M_{\odot}$. With gas mass and SFR estimates in hand, gas depletion timescales can be derived in a statistical sense for the sample overall. We find gas depletion times around $\tau \sim 200 \text{ Myr}$ with median and standard deviation $\tau = 220 \pm 70 \text{ Myr}$, consistent with the majority of $z \gtrsim 1$ DSFGs (e.g. Swinbank et al. 2014; Dudzevičiūtė et al. 2020; Sun et al. 2021).

The best fit SEDs are presented with photometry overplotted in Figure 4, with best fit parameters listed in Table 2.

4. DISCUSSION

Taking an accurate census of DSFGs at early epochs is crucial to understanding not only their contributions to dust, metals, and star formation within the first few Gyr, but also the assembly of massive galaxies ($M^* > 10^{11} M_{\odot}$) and large scale structure in the early Universe. DSFG halo masses are comparable or greater than that of quasar host galaxies at similar redshifts (e.g. Marone et al. 2018). While the number density of DSFGs is unconstrained at early epochs ($z > 4$), it may exceed that of rare quasars by $10 - 100 \times$, as starbursts are prolonged compared to quasar phases (e.g. Marconi et al. 2004). Characterizing the population of high- z DSFGs naturally enables the measurement of the contributions of low mass galaxies versus high mass galaxies like DSFGs and quasar host galaxies to the CSFRD.

The goals of this work have been to identify the highest- z sources from a sample of luminous DSFGs for further follow-up using 2 mm observations, characterize 2 mm emission and FIR SEDs for the sample, provide an independent measurement of the volume density of $z > 3$ DSFGs, and test the practical utility of 2 mm follow up observations as a useful and efficient redshift filter for large DSFG surveys. Based on FIR SED analysis for our galaxies, we place our sample into context with other DSFG populations, characterize the density of $850 \mu\text{m}$ -bright sources in the field, and evaluate the sample's contribution to the CSFRD.

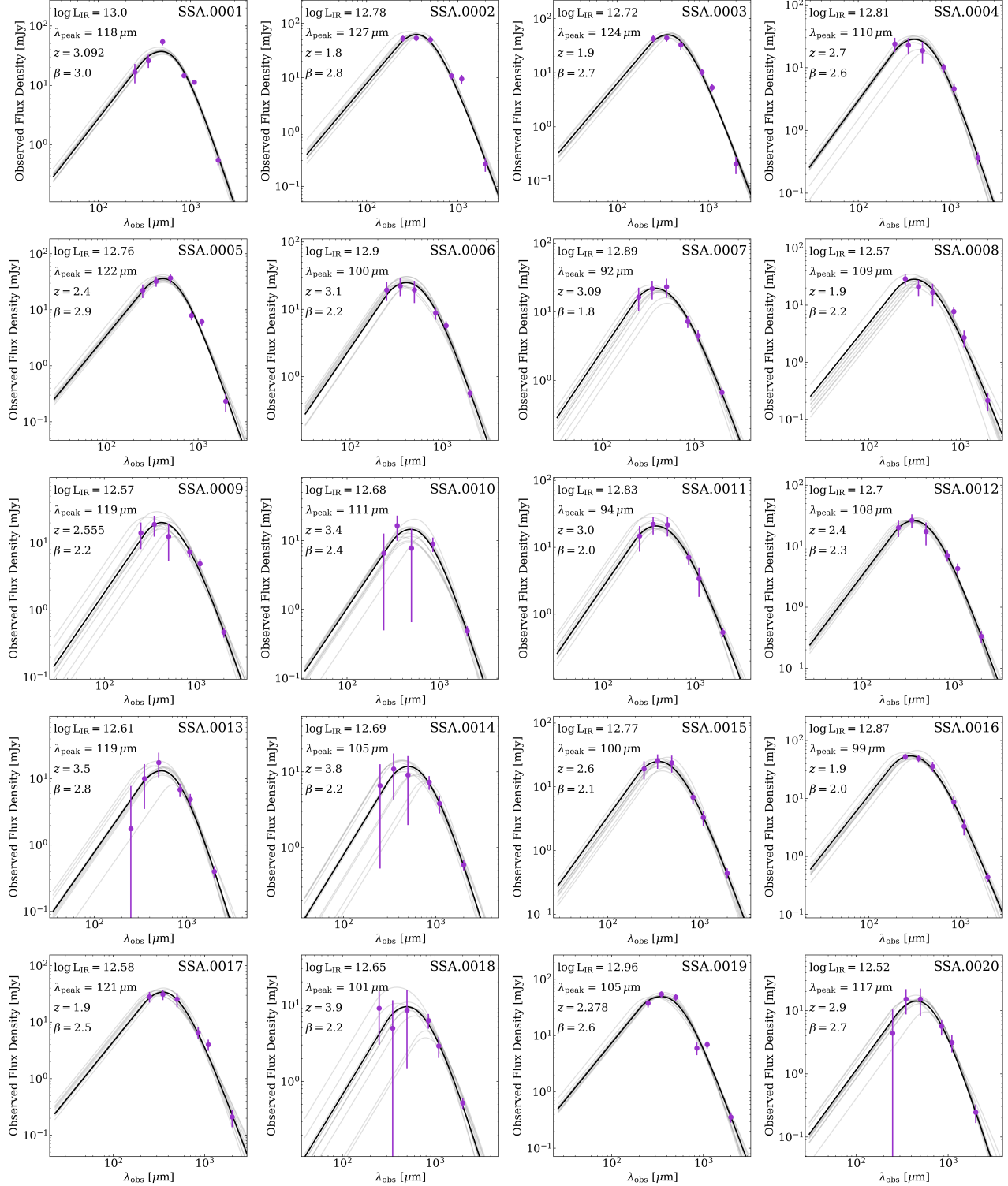
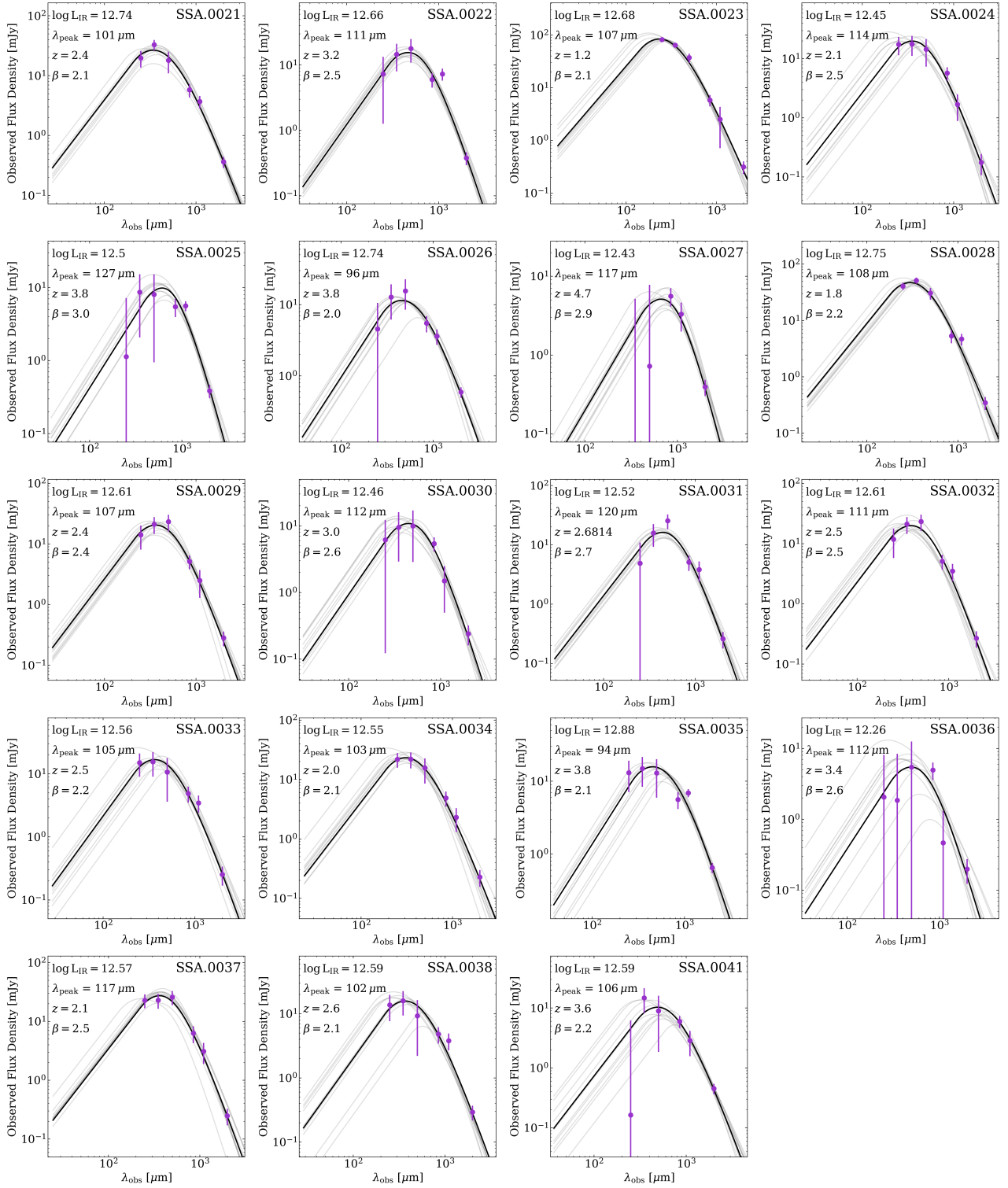


Figure 4: Millimeter photometry (purple points) with the best fit dust SED (black line) for each target in the sample. SEDs are constructed as a modified blackbody with a mid-infrared powerlaw component. For the modified blackbody we assume a general opacity such that $\tau = 1$ at $200 \mu\text{m}$, near the intrinsic peak of the dust SED. The uncertainty of the fit is shown via the gray SED fits, drawn randomly from the successful MCMC trials. Measured SED characteristics are noted for each target in their respective panels and given in Table 2.



— Continuation of Figure 4 —

4.1. Redshift Distribution of $S_{850\mu\text{m}} > 5.55 \text{ mJy}$ Sources

Based on the cumulative probability distribution function, $\sim 80\%$ of the aggregate probability density distribution is at $z > 2$. We categorize 15/39 galaxies as low- z , with a minimum redshift solution for an individual source of $z = 1.2^{+0.4}_{-0.4}$ for SSA.0023. We categorize 17/39 sources as potential protocluster members, or those most likely to be in the redshift range of the protocluster. Based on crossmatching as detailed in Section §2.3, we find most of our protocluster-binned sample has not been previously cataloged as protocluster members, nor are they expected to be members; rather they have a higher likelihood of being members than the DSFGs in low- z and high- z bins. Indeed, only $\sim 5\%$ of the volume representing the protocluster bin corresponds to the protocluster volume itself, leaving substantial room for our DSFGs to lie in the foreground or background population. Taking an overdensity of $\delta_{\text{rare}} = 10$ (Casey 2016) and the protocluster comoving volume within the S2CLS SSA22 coverage (assuming a redshift range informed by Topping et al. 2018) we may only expect $\sim 4 - 7$ of these sources to be protocluster members. Comparing our results to the typical density of $S_{850\mu\text{m}} > 5 \text{ mJy}$ sources in the field (Umehata et al. 2015), we find no statistical excess of sources in the protocluster bin; therefore, in the absence of spectroscopic confirmation, we cannot definitively classify these galaxies as protoclusters members. Lastly, we categorize 7/39 sources as high- z , with a maximum redshift solution for an individual source of $z = 4.7^{+3.6}_{-1.7}$ for SSA.0027. For the high- z sample, $\sim 60\%$ of the aggregate probability density distribution is at $z > 4$ (see Figure 2).

While the redshift distribution of galaxies selected at 2 mm is expected to be relatively high with $\langle z \rangle \approx 3.6$ (Casey et al. 2021), the selection of these targets at $850\mu\text{m}$ leads to a lower median redshift, consistent with what has been previously found for $850\mu\text{m}$ -selected DSFGs (e.g. Dudzevičiūtė et al. 2020; da Cunha et al. 2021). Therefore, though we expect the follow up 2 mm observations to filter out lower redshift sources (Casey et al. 2021; Zavala et al. 2021, Manning et al. submitted), for this study the redshift distribution is reflective of the $850\mu\text{m}$ -selection. Previous millimeter studies demonstrate that deeper surveys tend to select for lower redshift DSFGs; in other words brighter DSFGs tend to sit at higher redshifts (e.g. Béthermin et al. 2015). Though we focus on only the brightest subset of the population, we find a redshift distribution consistent with other $850\mu\text{m}$ -selected SMG samples.

We find a positive correlation between 2 mm flux density and redshift, and sources with lower flux ratios

$S_{850\mu\text{m}}/S_{2\text{mm}}$ tend to have higher redshifts (see Figure 5). The loose positive correlation between 2 mm flux density and redshift implies that 2 mm flux density alone does not constrain redshift, but does suggest sources with higher 2 mm flux densities tend to sit at higher redshifts. The relation between FIR/mm flux density and redshift becomes more clear with the flux ratio $S_{850\mu\text{m}}/S_{2\text{mm}}$; for a source with a given $850\mu\text{m}$ flux density, a relatively higher 2 mm flux density tends to result in a higher redshift solution. This trend holds for sources in our sample with MPPZ-derived redshifts as well as spectroscopic redshifts.

Our redshift distribution has good agreement with other $850/870\mu\text{m}$ -selected surveys, including Chapman et al. (2005), who conduct an early assessment of the $850\mu\text{m}$ -selected SMG redshift distribution (median $z = 2.2$), and Wardlow et al. (2011), with a similar redshift distribution peaking around $z \sim 2.5$ for their complete, unbiased $870\mu\text{m}$ -selected sample. Similarly, Danielson et al. (2017) derive a median redshift of $z = 2.4 \pm 0.1$ for the 52 spectroscopically confirmed SMGs in their sample. Danielson et al. (2017) also find the distribution features a high redshift tail, with $\sim 23\%$ of the SMGs at $z \geq 3$; we find a comparable $\sim 35\%$ of the sample at $z \geq 3$. The recent AS2UDS survey (Dudzevičiūtė et al. 2020) follow-up a comparable sample of $S_{850\mu\text{m}} > 3.6 \text{ mJy}$ SCUBA-2-selected SMGs in the UKIDSS UDS field with ALMA at $870\mu\text{m}$. They find a photometric redshift distribution with median $z = 2.61 \pm 0.08$ (1σ range of $z = 1.8 - 3.4$), in good agreement with our sample's median redshift of $z = 2.6 \pm 0.2$ (bootstrapped error on the median) and 1σ range of $z = 1.9 - 3.6$. In addition, they find $\sim 6\%$ of their sample at $z > 4$, and only 5/707 ($<< 1\%$) sources at $z < 1$. This is broadly consistent with our smaller, brighter sample, as we find zero sources at $z < 1$, and find one source ($\sim 3 \pm 3\%$ of the sample) formally at $z > 4$. Still, we do find a number of galaxies at $z > 3.8$ (6/39, most of the high- z sample).

We also find consistent results with the ALESS survey (da Cunha et al. 2021), a sample of 99 $870\mu\text{m}$ -selected SMGs followed up with ALMA 2 mm observations, with a similar flux density limit as AS2UDS of $S_{870} \geq 3.5 \text{ mJy}$. To compare to our sample, we take the subset of 25/99 ALESS sources with $S_{870} \geq 5 \text{ mJy}$ from da Cunha et al. (2021), and find a median redshift and 68% confidence interval of $z_{\text{med}} = 3.2^{+0.4}_{-1.1}$. This is broadly in agreement with our median redshift. Note that the full ALESS sample has a median redshift $z_{\text{med}} = 2.8^{+0.7}_{-0.8}$, and includes fainter sources than our sample selection criteria.

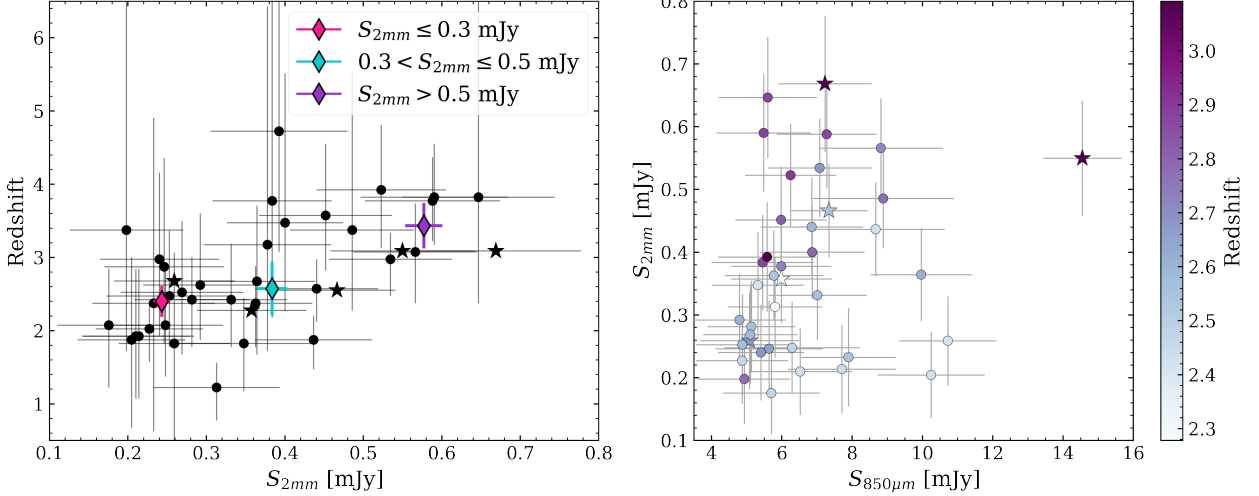


Figure 5: Redshift versus (sub)mm flux density for the $S_{850\mu\text{m}} > 5.55$ mJy sample. *Left:* Flux density $S_{2\text{mm}}$ versus redshift showing some positive correlation, with sources with higher $S_{2\text{mm}}$ tending to have higher redshift solutions. The stars indicate sources which have spectroscopic redshifts, otherwise `MMpz`-derived redshifts are shown. The average values within given flux density bins are shown as colored diamonds. *Right:* Flux densities $S_{2\text{mm}}$ versus $S_{850\mu\text{m}}$ with point color indicating redshift as shown by the colorbar on the right. As before, the stars denote spec- z 's while the circles are photo- z 's. Sources with lower flux ratios $S_{850\mu\text{m}}/S_{2\text{mm}}$ tend to sit at higher redshifts.

4.2. Utility of 2mm as a Redshift Filter

A key motivation in this work is to analyze the utility of 2mm in identifying the highest redshift galaxies among a population that lacks spectroscopy or high quality OIR photometric redshifts. This is a core problem in the study of obscured galaxy populations, where the search for redshifts has been the primary bottleneck for the past 20 years (Casey, Narayanan, & Cooray 2014). For example, following up these sources with spectral scans in the millimeter would take over 100 hours with ALMA (at least ~ 3 hours per source with overheads), versus the total time spent in this paper, with a total on-source time of just 34.12 min for 39 sources (< 1 min per source). Selection at 2mm has been found to effectively select a higher redshift population of DSFGs, as shown by the blind 2mm MORA survey in Casey et al. (2021), with $\langle z \rangle = 3.6^{+0.5}_{-0.9}$ for their sample. Our hypothesis is that 2mm imaging can provide an efficient and targeted method for identifying high- z candidates for follow-up as a zeroth order redshift sorting of $850\mu\text{m}$ -bright sources (limited to sources that are detected at $850\mu\text{m}$ by construction, given our selection criteria).

Definitively assessing the utility of 2mm imaging for redshift filtering requires spectroscopic redshifts, but in the absence of spectroscopic data we can evaluate the impact of 2mm data on our derivation of redshifts relative to the other bands for which we have data. To derive a photo- z , `MMpz` uses all flux densities for which

galaxies have measurements; is our redshift solution primarily driven by 2mm flux density, which would render the correlation of 2mm flux density and redshift in Figure 5 unsurprising?

To evaluate the set of photometry that has the most influence for `MMpz` redshift solutions, we generate simulated galaxy FIR/mm photometry. We specifically test the sensitivity of `MMpz` on the addition or absence of different bands by generating fake galaxies' SEDs using the same methodology as Casey (2020) where sources of different fixed redshifts are assigned realistic flux densities with associated uncertainties matched to those of this dataset. We then fit redshifts with `MMpz` for subsets of the data including the full data set: SPIRE 250 μm /350 μm /500 μm , SCUBA-2 850 μm , AzTEC 1.1 mm, ALMA 2 mm; just SCUBA-2 850 μm and ALMA 2 mm; and just SPIRE 250 μm /350 μm /500 μm and SCUBA-2 850 μm . Casey (2020) notes that using only 850 μm and 2mm photometry – two points that should exclusively probe the Rayleigh-Jeans tail for most redshifts and temperature – is insufficient. SPIRE 250 μm /350 μm /500 μm data is needed to constrain the dust peak for $z \lesssim 6$, where even non-detections provide very useful (though loose) constraints on the SED peak.

From these simulated SEDs, the addition of the 2mm point – provided $\sim 500\mu\text{m}$ constraints exist – improves accuracy from $\Delta z/(1+z) = 0.3$ (without the 2mm data) to $\Delta z/(1+z) = 0.2$ (with the 2mm data), in particular

Name	z_{MMPz}	z bin	z_{OIR}	z_{spec}	β	$\log L_{\text{IR}}$ $\log_{10}(L_{\odot})$	SFR $M_{\odot} \text{ yr}^{-1}$	λ_{peak} μm	T_{dust}^* K
SSA.0001	$3.3^{+2.8}_{-1.6}$	Protocluster	$2.85^{+3.15}_{-0.98}$	3.092 ^a	$3.0^{+0.2}_{-0.2}$	$13.00^{+0.06}_{-0.07}$	1480^{+230}_{-210}	118^{+7}_{-7}	41^{+3}_{-3}
SSA.0002	$1.8^{+1.2}_{-1.4}$	Low- z			$2.8^{+0.3}_{-0.2}$	$12.78^{+0.05}_{-0.05}$	890^{+110}_{-90}	127^{+7}_{-8}	36^{+4}_{-3}
SSA.0003	$1.9^{+1.1}_{-1.2}$	Low- z			$2.6^{+0.3}_{-0.2}$	$12.71^{+0.06}_{-0.06}$	770^{+110}_{-100}	124^{+9}_{-10}	37^{+4}_{-4}
SSA.0004	$2.5^{+1.2}_{-0.9}$	Protocluster			$3.42^{+0.06}_{-0.11}$	$12.81^{+0.09}_{-0.10}$	960^{+230}_{-200}	110^{+13}_{-12}	44^{+6}_{-6}
SSA.0005	$2.4^{+2.5}_{-1.8}$	Low- z	$3^{+1.27}_{-1.67}$		$3.0^{+0.3}_{-0.3}$	$12.76^{+0.07}_{-0.07}$	860^{+150}_{-130}	122^{+9}_{-9}	39^{+4}_{-4}
SSA.0006	$3.1^{+0.7}_{-0.7}$	Protocluster			$2.2^{+0.3}_{-0.3}$	$12.90^{+0.09}_{-0.11}$	1200^{+300}_{-300}	100^{+12}_{-11}	49^{+7}_{-6}
SSA.0007	$3.2^{+0.5}_{-0.5}$	Protocluster	$3.7^{+0.72}_{-0.19}$	3.0854 ^b	$1.9^{+0.3}_{-0.2}$	$12.89^{+0.11}_{-0.12}$	1200^{+300}_{-300}	92^{+11}_{-10}	53^{+7}_{-7}
SSA.0008	$1.9^{+0.9}_{-0.9}$	Low- z	$2.2^{+0.06}_{-0.05}$		$2.2^{+0.4}_{-0.4}$	$12.57^{+0.11}_{-0.12}$	550^{+200}_{-130}	109^{+18}_{-18}	44^{+11}_{-8}
SSA.0009	$3.1^{+0.9}_{-0.7}$	Protocluster	$2.2^{+0.72}_{-0.32}$	2.555 ^c	$2.2^{+0.3}_{-0.3}$	$12.57^{+0.12}_{-0.15}$	550^{+180}_{-160}	119^{+16}_{-13}	38^{+6}_{-7}
SSA.0010	$3.5^{+2.0}_{-1.2}$	Protocluster			$2.4^{+0.6}_{-0.5}$	$12.68^{+0.16}_{-0.20}$	700^{+300}_{-300}	111^{+22}_{-19}	43^{+10}_{-10}
SSA.0011	$3.0^{+0.4}_{-0.5}$	Protocluster			$2.0^{+0.3}_{-0.3}$	$12.83^{+0.11}_{-0.13}$	1000^{+300}_{-300}	94^{+13}_{-11}	52^{+8}_{-7}
SSA.0012	$2.4^{+0.8}_{-0.7}$	Low- z	$6^{+0}_{-4.06}$		$2.3^{+0.4}_{-0.3}$	$12.70^{+0.10}_{-0.10}$	750^{+200}_{-160}	108^{+13}_{-13}	44^{+7}_{-6}
SSA.0013	$3.5^{+2.0}_{-1.2}$	Protocluster	$2.55^{+3.45}_{-0.69}$		$2.8^{+0.4}_{-0.4}$	$12.61^{+0.15}_{-0.19}$	610^{+260}_{-220}	119^{+19}_{-16}	40^{+8}_{-8}
SSA.0014	$3.8^{+0.6}_{-0.6}$	High- z			$2.2^{+0.5}_{-0.4}$	$12.69^{+0.19}_{-0.25}$	730^{+400}_{-320}	105^{+25}_{-18}	46^{+11}_{-12}
SSA.0015	$2.6^{+0.4}_{-0.5}$	Protocluster			$2.1^{+0.4}_{-0.3}$	$12.78^{+0.10}_{-0.11}$	880^{+230}_{-190}	100^{+12}_{-12}	49^{+8}_{-6}
SSA.0016	$1.9^{+0.3}_{-0.4}$	Low- z			$2.0^{+0.3}_{-0.2}$	$12.87^{+0.09}_{-0.08}$	1100^{+300}_{-200}	99^{+11}_{-13}	49^{+8}_{-6}
SSA.0017	$1.9^{+0.9}_{-0.9}$	Low- z	$2.25^{+0.2}_{-0.4}$		$2.5^{+0.3}_{-0.3}$	$12.58^{+0.09}_{-0.08}$	570^{+130}_{-100}	121^{+12}_{-13}	38^{+6}_{-5}
SSA.0018	$3.9^{+0.9}_{-0.8}$	High- z	$2.85^{+2.7}_{-0.69}$		$2.1^{+0.5}_{-0.4}$	$12.64^{+0.23}_{-0.28}$	700^{+400}_{-300}	101^{+27}_{-20}	48^{+14}_{-13}
SSA.0019	$2.1^{+1.5}_{-1.5}$	Low- z	$2.15^{+0.23}_{-0.21}$	2.278 ^d	$2.8^{+0.3}_{-0.2}$	$13.0^{+0.06}_{-0.06}$	1400^{+200}_{-200}	105^{+8}_{-8}	47^{+5}_{-4}
SSA.0020	$2.9^{+1.5}_{-1.1}$	Protocluster			$2.7^{+0.5}_{-0.5}$	$12.52^{+0.15}_{-0.18}$	490^{+200}_{-170}	117^{+17}_{-18}	41^{+9}_{-8}
SSA.0021	$2.3^{+0.6}_{-0.6}$	Low- z	$3.3^{+0.19}_{-0.21}$		$2.2^{+0.3}_{-0.3}$	$12.74^{+0.10}_{-0.10}$	820^{+220}_{-170}	101^{+12}_{-13}	48^{+8}_{-6}
SSA.0022	$3.2^{+3.3}_{-1.5}$	Protocluster			$2.5^{+0.4}_{-0.4}$	$12.66^{+0.15}_{-0.17}$	690^{+280}_{-230}	111^{+18}_{-16}	44^{+9}_{-8}
SSA.0023	$1.2^{+0.3}_{-0.5}$	Low- z			$2.1^{+0.3}_{-0.3}$	$12.68^{+0.14}_{-0.10}$	710^{+280}_{-150}	107^{+14}_{-16}	44^{+10}_{-6}
SSA.0024	$2.1^{+0.8}_{-0.9}$	Low- z			$2.5^{+0.5}_{-0.5}$	$12.45^{+0.16}_{-0.15}$	420^{+180}_{-120}	114^{+20}_{-23}	42^{+13}_{-9}
SSA.0025	$3.8^{+3.5}_{-1.6}$	High- z			$3.0^{+0.4}_{-0.5}$	$12.50^{+0.21}_{-0.21}$	470^{+280}_{-190}	127^{+20}_{-22}	36^{+10}_{-9}
SSA.0026	$3.8^{+0.7}_{-0.7}$	High- z			$2.0^{+0.4}_{-0.3}$	$12.74^{+0.18}_{-0.24}$	810^{+410}_{-340}	96^{+20}_{-15}	51^{+11}_{-11}
SSA.0027	$4.7^{+3.6}_{-1.7}$	High- z			$2.9^{+0.4}_{-0.6}$	$12.43^{+0.22}_{-0.24}$	410^{+270}_{-170}	117^{+20}_{-23}	41^{+12}_{-9}
SSA.0028	$1.8^{+0.6}_{-0.7}$	Low- z	$0^{+0.01}_{-0} \dagger$		$2.2^{+0.3}_{-0.3}$	$12.75^{+0.08}_{-0.07}$	830^{+170}_{-120}	108^{+10}_{-12}	45^{+6}_{-5}
SSA.0029	$2.4^{+0.6}_{-0.6}$	Low- z			$2.6^{+0.4}_{-0.4}$	$12.61^{+0.12}_{-0.13}$	610^{+200}_{-160}	107^{+15}_{-16}	45^{+9}_{-7}
SSA.0030	$3.0^{+1.2}_{-1.1}$	Protocluster			$2.6^{+0.5}_{-0.6}$	$12.46^{+0.20}_{-0.26}$	430^{+260}_{-190}	112^{+25}_{-23}	43^{+13}_{-12}
SSA.0031	$2.8^{+2.8}_{-1.5}$	Protocluster		2.6814 ^e	$2.7^{+0.5}_{-0.5}$	$12.56^{+0.13}_{-0.15}$	540^{+190}_{-160}	116^{+14}_{-16}	41^{+8}_{-7}
SSA.0032	$2.5^{+1.0}_{-0.8}$	Protocluster	$1.75^{+4.25}_{-0.82}$		$2.7^{+0.4}_{-0.4}$	$12.61^{+0.12}_{-0.13}$	610^{+200}_{-160}	111^{+15}_{-16}	44^{+9}_{-7}
SSA.0033	$2.5^{+0.8}_{-0.8}$	Protocluster			$2.1^{+0.5}_{-0.4}$	$12.56^{+0.16}_{-0.18}$	540^{+250}_{-180}	105^{+20}_{-19}	46^{+12}_{-10}
SSA.0034	$2.0^{+0.4}_{-0.5}$	Low- z	$2.05^{+0.32}_{-0.2}$		$2.1^{+0.4}_{-0.4}$	$12.55^{+0.15}_{-0.13}$	530^{+220}_{-140}	103^{+17}_{-19}	47^{+12}_{-8}
SSA.0035	$3.8^{+2.8}_{-1.5}$	High- z			$2.1^{+0.4}_{-0.4}$	$12.88^{+0.16}_{-0.23}$	1100^{+500}_{-500}	94^{+23}_{-14}	52^{+10}_{-12}
SSA.0036	3^{+5}_{-2}	High- z			$2.6^{+0.6}_{-0.7}$	$12.3^{+0.3}_{-0.4}$	270^{+270}_{-160}	110^{+30}_{-30}	43^{+18}_{-14}
SSA.0037	$2.1^{+0.7}_{-0.7}$	Low- z			$2.5^{+0.5}_{-0.4}$	$12.57^{+0.11}_{-0.10}$	550^{+150}_{-110}	117^{+15}_{-19}	40^{+9}_{-7}
SSA.0038	$2.6^{+1.0}_{-0.8}$	Protocluster			$2.1^{+0.5}_{-0.4}$	$12.59^{+0.16}_{-0.18}$	570^{+260}_{-200}	102^{+19}_{-18}	47^{+12}_{-10}
SSA.0041	$3.6^{+1.0}_{-0.8}$	Protocluster			$2.2^{+0.5}_{-0.4}$	$12.59^{+0.19}_{-0.26}$	600^{+300}_{-300}	106^{+25}_{-18}	45^{+11}_{-12}

Table 2: Measured and derived characteristics for each galaxy in our sample. Photometric redshift results from MMPz are listed in z_{MMPz} , with OIR photometric redshifts quoted as given in Umehata et al. (2014) under z_{OIR} , and any literature spec- z values listed in z_{spec} with the reference (a: Umehata et al. (2014), b: Kubo et al. (2016), c: Chapman et al. (2005), d: Alaghband-Zadeh et al. (2012), e: Cooper et al. in prep). Measured from the best fit SEDs (see Figure 4) are emissivity spectral index β , IR luminosity $\log L_{\text{IR}}$, dust temperature T_{dust} , and peak wavelength λ_{peak} . The star formation rates (SFR) are derived from L_{IR} using the Kennicutt & Evans (2012) scaling. *Note that we assume a general opacity such that $\tau = 1$ at 200 μm , therefore these estimates are only comparable to other works using a similar model. †Reported z_{OIR} from Umehata et al. (2014), which we note is inconsistent with both our FIR results and OIR archival data (see discussion of the source in §3.1).

for galaxies at $z \gtrsim 3.5$. This demonstrates that given *Herschel* data, the 2 mm data is the next most impactful data for improved accuracy of the redshift solution, especially for high redshift sources. For example, the probability of a hypothetical source with $z_{\text{MMp}z} = 4.1$ lying at $z > 3.5$ increases from 81% without the 2 mm constraint, to 96% with the 2 mm constraint.

While 2 mm data does improve the accuracy of redshift constraints, they do not significantly change the precision of those redshift solutions. Quantitatively, the average breadth of redshift PDFs for our sample is $\delta z = 1.1 - 1.2$ with or without the 2 mm data folded into the photometry. This is not unexpected, as the breadth of the redshift PDF generated from millimeter data is dominated by the intrinsic spread in the $L_{\text{IR}}-\lambda_{\text{peak}}$ relation (discussed further in Casey 2020).

4.3. Emissivity Spectral Index β

With 2 mm flux densities in hand for a large sample of bright 850 μm -selected DSFGs, we have a unique dataset with which we analyze the galaxy-integrated slope of the Rayleigh-Jeans tail of blackbody emission. The slope is governed by the physical quantity β , the emissivity spectral index, or the frequency dependence of dust grain emissivity per unit mass. Still, drawing a physical interpretation for a measured β is not possible for spatially unresolved high redshift galaxies due to the complexity and heterogeneity of the ISM. This is especially true for sources lacking secure redshifts and with somewhat limited FIR/mm photometry.

Nevertheless, our data can be used to compare galaxy-integrated Rayleigh-Jeans slopes to other high- z samples and commonly adopted literature values of β for high- z datasets of similar quality. Here, our finding of $\langle \beta \rangle = 2.4^{+0.4}_{-0.3}$ suggests that the distribution of integrated β indices skews high, in line with other recent works, including a well-studied galaxy in SSA22 with $\beta = 2.3$ (Kato et al. 2018) as well as other samples with dust continuum data at $\lambda_{\text{obs}} \gtrsim 2 \text{ mm}$ (Jin et al. 2019; Casey et al. 2021). The aggregate best fit SED results for our sample (see Table 2) shows relatively steep β values ranging from $1.8 < \beta < 3.0$, all steeper than the standard value often adopted in the literature, typically $\beta = 1.8$ (e.g. Scoville et al. 2016), justified by measurements of the β from Milky Way's ISM (e.g. Paradis et al. 2009; Planck Collaboration et al. 2011). Nevertheless, while our median β skews high at $\langle \beta \rangle = 2.4^{+0.4}_{-0.3}$, it remains consistent with theoretical predictions for interstellar dust models (e.g. Draine & Lee 1984; Köhler et al. 2015), which predict $1 < \beta < 2.5$ depending on grain composition.

Figure 6 indicates the millimeter color distribution for the sample, represented by observed flux density ratio $S_{850 \mu\text{m}}/S_{2 \text{ mm}}$. We compare the millimeter colors to SED tracks constructed from a modified blackbody with mid-infrared power law spanning $1.8 < \beta < 3.0$ and $90 \mu\text{m} < \lambda_{\text{peak}} < 120 \mu\text{m}$. The sources follow a general trend of $S_{850 \mu\text{m}}/S_{2 \text{ mm}}$ with redshift aligned with the shape of the model SEDs. Though this trend may be due to the use of millimeter photometry to derive redshifts, we note that MMp z fixes $\beta = 1.8$ and that modifications of β do not significantly impact the output redshift probability density distributions. The majority of sources have flux density ratios suggestive of high $\beta > 1.8$, with the sample largely consistent with SED tracks for $\beta \approx 2.0 - 2.5$ (cyan and purple tracks in Figure 6). This aggregate high β result suggests that steeper Rayleigh-Jeans slopes, i.e. higher β , should likely be applied for similar high- z DSFGs in the literature in future works.

We further test our results by fitting the IR SEDs to a modified blackbody using MAGPHYS (da Cunha et al. 2008) as applied in da Cunha et al. (2021). Given the known degeneracies and bias from opacity assumptions, we toggled λ_0 over multiple fits. For $\lambda_0 = 200 \mu\text{m}$, we find a median of $\beta = 2.1 \pm 0.5$, statistically consistent within error with our previous result. Note that while in both SED fitting routines we assume isothermal dust, a primary difference between methods is the Drew et al. (in prep) model accounts for the range in temperature on Wien's portion of the SED with a power-law, whereas MAGPHYS accounts for this by not attempting to fit any points below 70 μm rest-frame. The discrepancy in results from these two methods demonstrates that care should be taken when directly comparing emissivity spectral indices obtained using different fitting methods. To this point, using identical fitting methods we do find a higher median emissivity spectral index for our sample ($\beta = 2.1 \pm 0.5$) than the ALESS sample ($\beta = 1.9 \pm 0.4$) da Cunha et al. (2021).

Though we have accounted for confusion noise as best as possible by using deboosted flux densities from SCUBA-2, measuring a higher β due to combining single dish 850 μm data with interferometric ALMA 2 mm data is a concern. Still, da Cunha et al. (2021) use multiwavelength ALMA data and demonstrate $\beta \approx 2$ for high- z DSFGs, with a median $\beta = 1.9 \pm 0.4$ derived for their sample. It is possible the bias from single dish data could be responsible for the difference between a $\beta \approx 2$ result and our higher $\beta \approx 2.4$ measurement. Large samples with redshifts and all ALMA data on the Rayleigh-Jeans tail are needed to take better measurements with

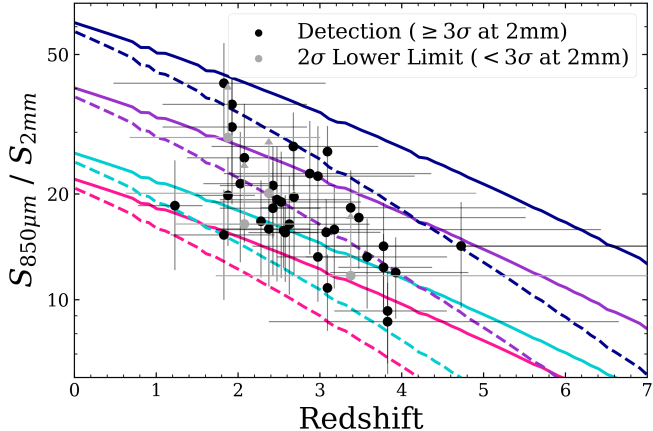


Figure 6: Flux density ratio $S_{850\mu\text{m}}/S_{2\text{mm}}$ versus redshift for the full sample; while $850\mu\text{m}$ flux densities are SCUBA-2 based, they have been deboosted for confusion noise and the errors here reflect that additional source of uncertainty. Redshifts are mm-derived from our analysis in all but five cases where a spec- z is available. Detected targets at 2 mm are denoted as secure detections ($\geq 3\sigma$ at 2 mm, black points) or plotted as 2σ lower limits for non-detections (detected at $< 3\sigma$ at 2 mm, in gray). Overlaid as colored lines are SED tracks, each a modified blackbody with mid-infrared power law for a given combination of emissivity spectral index ($\beta = 1.8, 2.0, 2.5$, and 3.0 in pink, cyan, purple, and navy, respectively) and dust temperature (given here as the observable, λ_{peak}), with solid lines for $\lambda_{\text{peak}} = 90\mu\text{m}$ and dashed for $\lambda_{\text{peak}} = 120\mu\text{m}$. Our sample is largely consistent with steeper slopes consistent with SED tracks for $\beta \approx 2.0 - 2.5$, with some variation (the median β measured is 2.4).

respect to confusion noise and multiplicity in detected sources.

A steeper β could result from a fundamental difference in grain composition or size (Chihara et al. 2001; Mutschke et al. 2013; Inoue et al. 2020), although testing this would require probing the ISM with high spatial resolution and sensitivity. Many of the caveats influencing observed β measurements – including geometric effects, variations in optical depth, and temperature distributions – would flatten rather than steepen the SED at long wavelengths.

4.4. CSFRD Contribution

We determine the sample’s estimated contribution to the cosmic star formation rate density (CSFRD), as shown in Figure 7, to compare with other similar estimates of DSFG samples in the literature. While we do not expect the presence of the protocluster to impact

our measurements, we verify this by analyzing the relative density of our sources compared to field samples. CSFRD estimates are found using a 100-trial Monte Carlo (MC) to sample the redshift and SFR probability density distributions for each of the 39 SSA22 sources. We calculate a comoving volume over the survey area (S2CLS coverage of SSA22 spans 0.28 deg^2) and redshift range based on discrete redshift bins (from $1 < z < 5$ with width $\Delta z = 0.5$), then divide the total SFR of all DSFGs in our sample by that volume when their draws fall in the given z -bin. The total CSFRD is measured for each MC trial, and from these measurements we take the mean and standard deviation for all trials to find the estimate for the CSFRD contribution from $1 < z < 5$ for this $S_{850\mu\text{m}} > 5.55\text{ mJy}$ sample.

Given the overall rarity of $S_{850\mu\text{m}} > 5.55\text{ mJy}$ sources among DSFGs, we estimate the impact of cosmic variance, and of incompleteness due to shallower S2CLS data of SSA22 relative to other fields like the UDS (Geach et al. 2017) and COSMOS (Simpson et al. 2019) SCUBA-2 maps. We conduct MC trials to count the number of sources in randomly placed SSA22-sized areas (0.28 deg^2) over UDS (0.74 deg^2) and COSMOS (1.94 deg^2); the 1σ $850\mu\text{m}$ depths are 0.9 mJy for UDS, 1.2 mJy for COSMOS, and 1.2 mJy for SSA22. We first enforce the same criteria used to select our SSA22 sources for the COSMOS/UDS sources: $S_{850\mu\text{m}} > 5\text{ mJy}$ and $> 5\sigma$. A first round of MC trials is run directly from the COSMOS/UDS catalogs for sources that meet these criteria. In this round, we find an average of 62^{+24}_{-30} sources/SSA22-sized field. This exceeds the 39 observed sources in SSA22 by a factor of $1.6^{+0.6}_{-0.8}$; though suggestive of an underdensity of bright DSFGs in SSA22, this does not account for the higher RMS noise in SSA22 relative to UDS/COSMOS. Thus this factor is more representative of incompleteness. For the next round of trials, we artificially boost the RMS of the UDS/COSMOS maps using the RMS distribution of the SSA22 map to simulate the shallower SSA22 map. We do this by drawing RMS values from the SSA22 map at random positions. After this elevation of noise for the COSMOS/UDS samples, we find an expectation value of 44^{+13}_{-14} sources/SSA22-sized field fulfilling our bright DSFG criteria. This is in line with our observed number of 39 DSFGs.

From this sampling of UDS/COSMOS maps, we determine that our SSA22 sample is not cosmologically over- or under-dense, but it is incomplete by a factor of $1.6^{+0.6}_{-0.8}$. While this is consistent with being complete, it does reveal a systematic offset that impacts our results based on the depth of SSA22 SCUBA-2 coverage, thus we adjust our CSFRD measurement accordingly.

We also run similar MC trials on simulated data to compare to our observational results. With the semiempirical model from Popping et al. (2020), we count the number of $S_{850\mu\text{m}} > 5\text{ mJy}$ sources in randomly placed SSA22-sized areas (0.28 deg^2), and find 61^{+8}_{-15} sources/SSA22-sized field. From similar MC trials on SHARK light cone results (Lagos et al. 2020) we find 48^{+12}_{-9} sources/SSA22-sized field. These results are consistent with the observational results from UDS & COSMOS S2CLS, supporting our estimates of incompleteness and cosmic variance for our sample from the real data.

The resulting CSFRD estimate for our sample is shown in Figure 7. This estimate is compared to the expected contribution by obscured galaxies to the CSFRD drawn from the IR luminosity function (IRLF) constraints in Zavala et al. (2021). We compare directly to the expected CSFRD for $S_{850\mu\text{m}} > 5.55\text{ mJy}$ from their work, corresponding to the $S_{850\mu\text{m}} > 5\text{ mJy}$ and $> 5\sigma$ selection for our sample at the 1σ depth ($\sim 1.2\text{ mJy}$) of the S2CLS data for SSA22. As shown in Figure 7, our incompleteness-corrected results are consistent with the Zavala et al. (2021) IRLF model within uncertainties.

Although we enforce a higher flux density cutoff than their sample, CSFRD estimates for our sample are comparable to those for the AS2UDS sample (Dudzevičiūtė et al. 2020). For our sample, we find the contribution to the CSFRD peaks around $z \sim 2.4$, slightly higher redshift than the total CSFRD peak at $z \sim 2$ from Madau & Dickinson (2014). Our $850\mu\text{m}$ -bright, obscured sources contribute $\sim 10\%$ (ranging 8–13%) to the cosmic-averaged CSFRD from $2 < z < 5$.

5. SUMMARY

In this paper we present ALMA 2mm imaging for a complete sample of 39 SCUBA-2 detected DSFGs in SSA22 selected for $S_{850\mu\text{m}} > 5\text{ mJy}$ at $> 5\sigma$ in S2CLS. We detect 35/39 sources at $S_{2\text{mm}} > 3\sigma$, where our sensitivity is $0.08\text{ mJy beam}^{-1}$ on average. With multi-wavelength (sub)millimeter data for the sample from *Herschel*/SPIRE, SCUBA-2, AzTEC, and ALMA, we characterize IR SEDs and measure and derive properties including IR luminosity, star formation rate, and emissivity spectral index. For each galaxy, we also estimate a millimeter photometric redshift with **MMpz**. Our main results are as follows:

- Based on our photometric redshifts and literature spectroscopic redshifts, we find a redshift distribution consistent with other $850\mu\text{m}$ -selected SMG samples, with $z_{\text{med}} = 2.6 \pm 0.7$ despite these sources being representative of only the brightest subset of the $850\mu\text{m}$ -selected population (often

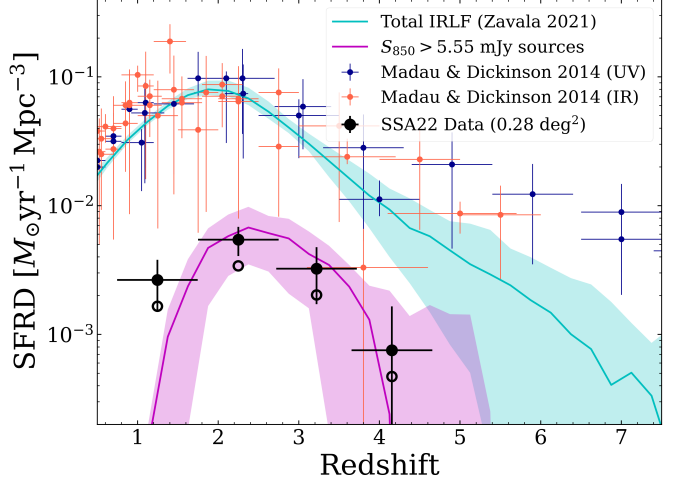


Figure 7: CSFRD as measured at rest-frame UV (blue) and IR-mm (orange) from Madau & Dickinson (2014). While rest-frame UV measurements now reach $z > 10$ thanks to deep HST NIR imaging campaigns, in contrast, surveys of obscured emission in galaxies remain uncertain at $z > 5$. The black points show the data, which lacks precision to constrain the CSFRD at high- z . The cyan region shows the IRLF from Zavala et al. (2021), and the magenta region shows the expected IRLF for sources with $S_{850\mu\text{m}} > 5.55\text{ mJy}$, corresponding to the $S_{850\mu\text{m}} > 5\text{ mJy}$ and $> 5\sigma$ selection for our sample at the SSA22 S2CLS depth. The filled black points show the CSFRD estimates from our SSA22 data corrected for incompleteness, while the open circles are the same data without correcting for incompleteness.

hypothesized to sit at higher redshifts). We also categorize 7/39 sources as high- z (all with redshift solutions $z \gtrsim 3.5$), to be spectroscopically confirmed in future follow-up observations.

- Provided the existence of $250 - 500\mu\text{m}$ photometry (i.e. from SPIRE) that brackets the dust SED peak for the majority of DSFGs, we find that the 2mm photometric constraints are the next most impactful for refining redshift solutions for these sources. With available redshift constraints, we generally find a positive correlation between redshift and 2mm flux density. This 2mm data point is especially useful for high redshift sources at $z > 3.5$, where the addition of the 2mm point improves accuracy from $\Delta z/(1+z) = 0.3$ (without the 2mm data) to $\Delta z/(1+z) = 0.2$ (with the 2mm data).
- Our sample has broadly steep emissivity spectral indices with median $\beta = 2.4 \pm 0.3$. Still, while

the aggregate β skews high, measurements for any individual β would be improved with matched beam ALMA data at both frequencies, with respect to confusion noise and multiplicity in detected sources.

- For our sample of $850\mu\text{m}$ -bright sources, we estimate the contribution to the cosmic-averaged CS-FRD is $\sim 10\%$ (ranging 8-13%).

Our study employs 2 mm imaging to filter out lower redshift DSFGs, advancing efforts to take a complete census of DSFGs at early epochs. While we do find that sources with higher 2 mm flux densities tend to sit at higher redshifts, spectroscopic follow up is needed to verify the efficacy of the 2 mm redshift filtering technique. Future 2 mm follow up of large samples of DSFGs will be a useful tool to improve the efficiency of identifying the highest redshift obscured galaxies.

ACKNOWLEDGEMENTS

The authors would like to extend their gratitude to Mark Swinbank for providing SPIRE imaging, Hideki Umehata for sharing AzTEC 1.1 mm imaging and catalog data, and Claudia Lagos for providing SHARK model lightcone results. ORC thanks the UT Austin

Astronomy Department and the Cox Board of Trustees for support through the Dean’s Excellence Fellowship. CMC thanks the National Science Foundation for support through grants AST-1814034 and AST-2009577, and the Research Corporation for Science Advancement for a 2019 Cottrell Scholar Award, sponsored by IF/THEN, an initiative of Lyda Hill Philanthropies.

This paper makes use of the following ALMA data: ADS/JAO.ALMA#2019.1.00313.S. ALMA is a partnership of ESO (representing its member states), NSF (USA) and NINS (Japan), together with NRC (Canada), MOST and ASIAA (Taiwan), and KASI (Republic of Korea), in cooperation with the Republic of Chile. The Joint ALMA Observatory is operated by ESO, AUI/NRAO and NAOJ. The National Radio Astronomy Observatory is a facility of the National Science Foundation operated under cooperative agreement by Associated Universities, Inc.

This research made use of the following software: spyder (Raybaut 2009), astropy (Astropy Collaboration et al. 2018), Matplotlib (Hunter 2007), NumPy (van der Walt et al. 2011), SymPy (Meurer et al. 2017), SciPy (Virtanen et al. 2020), pandas (Wes McKinney 2010; pandas development team 2020).

REFERENCES

- Ahumada, R., Prieto, C. A., Almeida, A., et al. 2020, ApJS, 249, 3, doi: [10.3847/1538-4365/ab929e](https://doi.org/10.3847/1538-4365/ab929e)
- Alaghband-Zadeh, S., Chapman, S. C., Swinbank, A. M., et al. 2012, MNRAS, 424, 2232, doi: [10.1111/j.1365-2966.2012.21386.x](https://doi.org/10.1111/j.1365-2966.2012.21386.x)
- Aretxaga, I., Wilson, G. W., Aguilar, E., et al. 2011, MNRAS, 415, 3831, doi: [10.1111/j.1365-2966.2011.18989.x](https://doi.org/10.1111/j.1365-2966.2011.18989.x)
- Astropy Collaboration, Price-Whelan, A. M., Sipőcz, B. M., et al. 2018, AJ, 156, 123, doi: [10.3847/1538-3881/aabc4f](https://doi.org/10.3847/1538-3881/aabc4f)
- Bendo, G. J., Griffin, M. J., Bock, J. J., et al. 2013, MNRAS, 433, 3062, doi: [10.1093/mnras/stt948](https://doi.org/10.1093/mnras/stt948)
- Béthermin, M., De Breuck, C., Sargent, M., & Daddi, E. 2015, A&A, 576, L9, doi: [10.1051/0004-6361/201525718](https://doi.org/10.1051/0004-6361/201525718)
- Blain, A. W., Smail, I., Ivison, R. J., Kneib, J. P., & Frayer, D. T. 2002, Physics Reports, 369, 111, doi: [10.1016/S0370-1573\(02\)00134-5](https://doi.org/10.1016/S0370-1573(02)00134-5)
- Bouwens, R. J., Illingworth, G. D., Oesch, P. A., et al. 2015, ApJ, 803, 34, doi: [10.1088/0004-637X/803/1/34](https://doi.org/10.1088/0004-637X/803/1/34)
- Braatz, J. 2021, ALMA Cycle 8 2021 Proposer’s Guide, ALMA Doc. 8.2 v1.0
- Carilli, C. L., & Walter, F. 2013, ARA&A, 51, 105, doi: [10.1146/annurev-astro-082812-140953](https://doi.org/10.1146/annurev-astro-082812-140953)
- Casey, C. M. 2012, MNRAS, 425, 3094, doi: [10.1111/j.1365-2966.2012.21455.x](https://doi.org/10.1111/j.1365-2966.2012.21455.x)
- . 2016, ApJ, 824, 36, doi: [10.3847/0004-637X/824/1/36](https://doi.org/10.3847/0004-637X/824/1/36)
- . 2020, ApJ, 900, 68, doi: [10.3847/1538-4357/aba528](https://doi.org/10.3847/1538-4357/aba528)
- Casey, C. M., Hodge, J., Zavala, J. A., et al. 2018a, ApJ, 862, 78, doi: [10.3847/1538-4357/aacd11](https://doi.org/10.3847/1538-4357/aacd11)
- Casey, C. M., Narayanan, D., & Cooray, A. 2014, PhR, 541, 45, doi: [10.1016/j.physrep.2014.02.009](https://doi.org/10.1016/j.physrep.2014.02.009)
- Casey, C. M., Chapman, S. C., Beswick, R. J., et al. 2009, MNRAS, 399, 121, doi: [10.1111/j.1365-2966.2009.15291.x](https://doi.org/10.1111/j.1365-2966.2009.15291.x)
- Casey, C. M., Berta, S., Béthermin, M., et al. 2012a, ApJ, 761, 140, doi: [10.1088/0004-637X/761/2/140](https://doi.org/10.1088/0004-637X/761/2/140)
- . 2012b, ApJ, 761, 140, doi: [10.1088/0004-637X/761/2/140](https://doi.org/10.1088/0004-637X/761/2/140)
- Casey, C. M., Zavala, J. A., Spilker, J., et al. 2018b, ApJ, 862, 77, doi: [10.3847/1538-4357/aac82d](https://doi.org/10.3847/1538-4357/aac82d)
- Casey, C. M., Zavala, J. A., Aravena, M., et al. 2019, ApJ, 887, 55, doi: [10.3847/1538-4357/ab52ff](https://doi.org/10.3847/1538-4357/ab52ff)
- Casey, C. M., Zavala, J. A., Manning, S. M., et al. 2021, arXiv e-prints, arXiv:2110.06930, <https://arxiv.org/abs/2110.06930>
- Chapman, S. C., Blain, A. W., Smail, I., & Ivison, R. J. 2005, ApJ, 622, 772, doi: [10.1086/428082](https://doi.org/10.1086/428082)

- Chapman, S. C., Lewis, G. F., Scott, D., et al. 2001, ApJL, 548, L17, doi: [10.1086/318919](https://doi.org/10.1086/318919)
- Chapman, S. C., Scott, D., Windhorst, R. A., et al. 2004a, ApJ, 606, 85, doi: [10.1086/382778](https://doi.org/10.1086/382778)
- Chapman, S. C., Smail, I., Blain, A. W., & Ivison, R. J. 2004b, ApJ, 614, 671, doi: [10.1086/423833](https://doi.org/10.1086/423833)
- Chihara, H., Koike, C., & Tsuchiyama, A. 2001, PASJ, 53, 243, doi: [10.1093/pasj/53.2.243](https://doi.org/10.1093/pasj/53.2.243)
- Conley, A., Cooray, A., Vieira, J. D., et al. 2011, ApJL, 732, L35, doi: [10.1088/2041-8205/732/2/L35](https://doi.org/10.1088/2041-8205/732/2/L35)
- Cooray, A., Calanog, J., Wardlow, J. L., et al. 2014, ApJ, 790, 40, doi: [10.1088/0004-637X/790/1/40](https://doi.org/10.1088/0004-637X/790/1/40)
- Cowie, L. L., Gardner, J. P., Hu, E. M., et al. 1994, ApJ, 434, 114, doi: [10.1086/174709](https://doi.org/10.1086/174709)
- Cowie, L. L., Songaila, A., Hu, E. M., & Cohen, J. G. 1996, AJ, 112, 839, doi: [10.1086/118058](https://doi.org/10.1086/118058)
- da Cunha, E., Charlot, S., & Elbaz, D. 2008, MNRAS, 388, 1595, doi: [10.1111/j.1365-2966.2008.13535.x](https://doi.org/10.1111/j.1365-2966.2008.13535.x)
- da Cunha, E., Groves, B., Walter, F., et al. 2013, ApJ, 766, 13, doi: [10.1088/0004-637X/766/1/13](https://doi.org/10.1088/0004-637X/766/1/13)
- da Cunha, E., Walter, F., Smail, I. R., et al. 2015, ApJ, 806, 110, doi: [10.1088/0004-637X/806/1/110](https://doi.org/10.1088/0004-637X/806/1/110)
- da Cunha, E., Hodge, J. A., Casey, C. M., et al. 2021, arXiv e-prints, arXiv:2106.08566.
<https://arxiv.org/abs/2106.08566>
- Danielson, A. L. R., Swinbank, A. M., Smail, I., et al. 2017, ApJ, 840, 78, doi: [10.3847/1538-4357/aa6caf](https://doi.org/10.3847/1538-4357/aa6caf)
- Draine, B. T., & Lee, H. M. 1984, ApJ, 285, 89, doi: [10.1086/162480](https://doi.org/10.1086/162480)
- Dudzevičiūtė, U., Smail, I., Swinbank, A. M., et al. 2020, MNRAS, 494, 3828, doi: [10.1093/mnras/staa769](https://doi.org/10.1093/mnras/staa769)
- Dunlop, J. S., McLure, R. J., Biggs, A. D., et al. 2017, MNRAS, 466, 861, doi: [10.1093/mnras/stw3088](https://doi.org/10.1093/mnras/stw3088)
- Eales, S., Lilly, S., Webb, T., et al. 2000, AJ, 120, 2244, doi: [10.1086/316823](https://doi.org/10.1086/316823)
- Ellis, R. S., McLure, R. J., Dunlop, J. S., et al. 2013, ApJL, 763, L7, doi: [10.1088/2041-8205/763/1/L7](https://doi.org/10.1088/2041-8205/763/1/L7)
- Finkelstein, S. L. 2016, PASA, 33, e037, doi: [10.1017/pasa.2016.26](https://doi.org/10.1017/pasa.2016.26)
- Finkelstein, S. L., Ryan, Russell E., J., Papovich, C., et al. 2015, ApJ, 810, 71, doi: [10.1088/0004-637X/810/1/71](https://doi.org/10.1088/0004-637X/810/1/71)
- Geach, J. E., Matsuda, Y., Smail, I., et al. 2005, MNRAS, 363, 1398, doi: [10.1111/j.1365-2966.2005.09538.x](https://doi.org/10.1111/j.1365-2966.2005.09538.x)
- Geach, J. E., Dunlop, J. S., Halpern, M., et al. 2017, MNRAS, 465, 1789, doi: [10.1093/mnras/stw2721](https://doi.org/10.1093/mnras/stw2721)
- Greve, T. R., Vieira, J. D., Weiβ, A., et al. 2012, ApJ, 756, 101, doi: [10.1088/0004-637X/756/1/101](https://doi.org/10.1088/0004-637X/756/1/101)
- Gruppioni, C., Pozzi, F., Rodighiero, G., et al. 2013, MNRAS, 432, 23, doi: [10.1093/mnras/stt308](https://doi.org/10.1093/mnras/stt308)
- Gruppioni, C., Béthermin, M., Loiacono, F., et al. 2020, A&A, 643, A8, doi: [10.1051/0004-6361/202038487](https://doi.org/10.1051/0004-6361/202038487)
- Hao, C.-N., Kennicutt, R. C., Johnson, B. D., et al. 2011, ApJ, 741, 124, doi: [10.1088/0004-637X/741/2/124](https://doi.org/10.1088/0004-637X/741/2/124)
- Hayashino, T., Matsuda, Y., Tamura, H., et al. 2004, AJ, 128, 2073, doi: [10.1086/424935](https://doi.org/10.1086/424935)
- Hodge, J. A., Karim, A., Smail, I., et al. 2013, ApJ, 768, 91, doi: [10.1088/0004-637X/768/1/91](https://doi.org/10.1088/0004-637X/768/1/91)
- Hughes, D. H., Serjeant, S., Dunlop, J., et al. 1998, Nature, 394, 241, doi: [10.1038/28328](https://doi.org/10.1038/28328)
- Hunter, J. D. 2007, Computing in Science Engineering, 9, 90, doi: [10.1109/MCSE.2007.55](https://doi.org/10.1109/MCSE.2007.55)
- Inoue, A. K., Hashimoto, T., Chihara, H., & Koike, C. 2020, MNRAS, 495, 1577, doi: [10.1093/mnras/staa1203](https://doi.org/10.1093/mnras/staa1203)
- Jin, S., Daddi, E., Magdis, G. E., et al. 2019, ApJ, 887, 144, doi: [10.3847/1538-4357/ab55d6](https://doi.org/10.3847/1538-4357/ab55d6)
- Kato, Y., Matsuda, Y., Smail, I., et al. 2016, MNRAS, 460, 3861, doi: [10.1093/mnras/stw1237](https://doi.org/10.1093/mnras/stw1237)
- Kato, Y., Matsuda, Y., Iono, D., et al. 2018, PASJ, 70, L6, doi: [10.1093/pasj/psy087](https://doi.org/10.1093/pasj/psy087)
- Kennicutt, R. C., & Evans, N. J. 2012, ARA&A, 50, 531, doi: [10.1146/annurev-astro-081811-125610](https://doi.org/10.1146/annurev-astro-081811-125610)
- Köhler, M., Ysard, N., & Jones, A. P. 2015, A&A, 579, A15, doi: [10.1051/0004-6361/201525646](https://doi.org/10.1051/0004-6361/201525646)
- Koprowski, M. P., Dunlop, J. S., Michałowski, M. J., et al. 2017, MNRAS, 471, 4155, doi: [10.1093/mnras/stx1843](https://doi.org/10.1093/mnras/stx1843)
- Kovács, A., Omont, A., Beelen, A., et al. 2010, ApJ, 717, 29, doi: [10.1088/0004-637X/717/1/29](https://doi.org/10.1088/0004-637X/717/1/29)
- Kroupa, P. 2001, MNRAS, 322, 231, doi: [10.1046/j.1365-8711.2001.04022.x](https://doi.org/10.1046/j.1365-8711.2001.04022.x)
- Kubo, M., Yamada, T., Ichikawa, T., et al. 2016, MNRAS, 455, 3333, doi: [10.1093/mnras/stv2392](https://doi.org/10.1093/mnras/stv2392)
- Lagos, C. d. P., da Cunha, E., Robotham, A. S. G., et al. 2020, MNRAS, 499, 1948, doi: [10.1093/mnras/staa2861](https://doi.org/10.1093/mnras/staa2861)
- Le Floc'h, E., Papovich, C., Dole, H., et al. 2005, ApJ, 632, 169, doi: [10.1086/432789](https://doi.org/10.1086/432789)
- Lee, N., Sanders, D. B., Casey, C. M., et al. 2013, ApJ, 778, 131, doi: [10.1088/0004-637X/778/2/131](https://doi.org/10.1088/0004-637X/778/2/131)
- Lehmer, B. D., Alexander, D. M., Chapman, S. C., et al. 2009, MNRAS, 400, 299, doi: [10.1111/j.1365-2966.2009.15449.x](https://doi.org/10.1111/j.1365-2966.2009.15449.x)
- Lewis, A. J. R., Ivison, R. J., Best, P. N., et al. 2018, ApJ, 862, 96, doi: [10.3847/1538-4357/aacc25](https://doi.org/10.3847/1538-4357/aacc25)
- Madau, P., & Dickinson, M. 2014, Annual Review of Astronomy & Astrophysics, 52, 415, doi: [10.1146/annurev-astro-081811-125615](https://doi.org/10.1146/annurev-astro-081811-125615)
- Magnelli, B., Elbaz, D., Chary, R. R., et al. 2011, A&A, 528, A35, doi: [10.1051/0004-6361/200913941](https://doi.org/10.1051/0004-6361/200913941)
- Magnelli, B., Popesso, P., Berta, S., et al. 2013, A&A, 553, A132, doi: [10.1051/0004-6361/201321371](https://doi.org/10.1051/0004-6361/201321371)

- Magnelli, B., Karim, A., Staguhn, J., et al. 2019, ApJ, 877, 45, doi: [10.3847/1538-4357/ab1912](https://doi.org/10.3847/1538-4357/ab1912)
- Marconi, A., Risaliti, G., Gilli, R., et al. 2004, MNRAS, 351, 169, doi: [10.1111/j.1365-2966.2004.07765.x](https://doi.org/10.1111/j.1365-2966.2004.07765.x)
- Marrone, D. P., Spilker, J. S., Hayward, C. C., et al. 2018, Nature, 553, 51, doi: [10.1038/nature24629](https://doi.org/10.1038/nature24629)
- Matsuda, Y., Yamada, T., Hayashino, T., et al. 2004, AJ, 128, 569, doi: [10.1086/422020](https://doi.org/10.1086/422020)
- . 2011, MNRAS, 410, L13, doi: [10.1111/j.1745-3933.2010.00969.x](https://doi.org/10.1111/j.1745-3933.2010.00969.x)
- Meurer, A., Smith, C. P., Paprocki, M., et al. 2017, PeerJ Computer Science, 3, e103, doi: [10.7717/peerj-cs.103](https://doi.org/10.7717/peerj-cs.103)
- Miettinen, O., Delvecchio, I., Smolčić, V., et al. 2017, A&A, 606, A17, doi: [10.1051/0004-6361/201730762](https://doi.org/10.1051/0004-6361/201730762)
- Miller, T. B., Hayward, C. C., Chapman, S. C., & Behroozi, P. S. 2015, MNRAS, 452, 878, doi: [10.1093/mnras/stv1267](https://doi.org/10.1093/mnras/stv1267)
- Murphy, E. J., Chary, R. R., Dickinson, M., et al. 2011, ApJ, 732, 126, doi: [10.1088/0004-637X/732/2/126](https://doi.org/10.1088/0004-637X/732/2/126)
- Mutschke, H., Zeidler, S., & Chihara, H. 2013, Earth, Planets, and Space, 65, 1139, doi: [10.5047/eps.2013.07.003](https://doi.org/10.5047/eps.2013.07.003)
- Nguyen, H. T., Schulz, B., Levenson, L., et al. 2010, A&A, 518, L5, doi: [10.1051/0004-6361/201014680](https://doi.org/10.1051/0004-6361/201014680)
- Oesch, P. A., Bouwens, R. J., Illingworth, G. D., et al. 2013, ApJ, 773, 75, doi: [10.1088/0004-637X/773/1/75](https://doi.org/10.1088/0004-637X/773/1/75)
- Overzier, R. A. 2016, A&A Rv, 24, 14, doi: [10.1007/s00159-016-0100-3](https://doi.org/10.1007/s00159-016-0100-3)
- pandas development team, T. 2020, pandas-dev/pandas: Pandas, latest, Zenodo, doi: [10.5281/zenodo.3509134](https://doi.org/10.5281/zenodo.3509134)
- Paradis, D., Bernard, J. P., & Mény, C. 2009, A&A, 506, 745, doi: [10.1051/0004-6361/200811246](https://doi.org/10.1051/0004-6361/200811246)
- Pilbratt, G. L., Riedinger, J. R., Passvogel, T., et al. 2010, A&A, 518, L1, doi: [10.1051/0004-6361/201014759](https://doi.org/10.1051/0004-6361/201014759)
- Planck Collaboration, Abergel, A., Ade, P. A. R., et al. 2011, A&A, 536, A25, doi: [10.1051/0004-6361/201116483](https://doi.org/10.1051/0004-6361/201116483)
- Planck Collaboration, Ade, P. A. R., Aghanim, N., et al. 2016, A&A, 594, A13, doi: [10.1051/0004-6361/201525830](https://doi.org/10.1051/0004-6361/201525830)
- Popping, G., Walter, F., Behroozi, P., et al. 2020, ApJ, 891, 135, doi: [10.3847/1538-4357/ab76c0](https://doi.org/10.3847/1538-4357/ab76c0)
- Raybaut, P. 2009, Available online at: pythonhosted.org
- Reuter, C., Vieira, J. D., Spilker, J. S., et al. 2020, ApJ, 902, 78, doi: [10.3847/1538-4357/abb599](https://doi.org/10.3847/1538-4357/abb599)
- Rowan-Robinson, M., Oliver, S., Wang, L., et al. 2016, MNRAS, 461, 1100, doi: [10.1093/mnras/stw1169](https://doi.org/10.1093/mnras/stw1169)
- Scott, K. S., Austermann, J. E., Perera, T. A., et al. 2008, MNRAS, 385, 2225, doi: [10.1111/j.1365-2966.2008.12989.x](https://doi.org/10.1111/j.1365-2966.2008.12989.x)
- Scoville, N., Sheth, K., Aussel, H., et al. 2016, ApJ, 820, 83, doi: [10.3847/0004-637X/820/2/83](https://doi.org/10.3847/0004-637X/820/2/83)
- Simpson, J. M., Smail, I., Swinbank, A. M., et al. 2015, ApJ, 807, 128, doi: [10.1088/0004-637X/807/2/128](https://doi.org/10.1088/0004-637X/807/2/128)
- . 2019, ApJ, 880, 43, doi: [10.3847/1538-4357/ab23ff](https://doi.org/10.3847/1538-4357/ab23ff)
- Simpson, J. M., Smail, I., Dudzevičiūtė, U., et al. 2020, MNRAS, 495, 3409, doi: [10.1093/mnras/staa1345](https://doi.org/10.1093/mnras/staa1345)
- Smail, I., Ivison, R. J., & Blain, A. W. 1997, ApJL, 490, L5, doi: [10.1086/311017](https://doi.org/10.1086/311017)
- Songaila, A., Cowie, L. L., Hu, E. M., & Gardner, J. P. 1994, ApJS, 94, 461, doi: [10.1086/192080](https://doi.org/10.1086/192080)
- Spilker, J. S., Marrone, D. P., Aravena, M., et al. 2016, ApJ, 826, 112, doi: [10.3847/0004-637X/826/2/112](https://doi.org/10.3847/0004-637X/826/2/112)
- Staguhn, J. G., Kovács, A., Arendt, R. G., et al. 2014, ApJ, 790, 77, doi: [10.1088/0004-637X/790/1/77](https://doi.org/10.1088/0004-637X/790/1/77)
- Steidel, C. C., Adelberger, K. L., Dickinson, M., et al. 1998, ApJ, 492, 428, doi: [10.1086/305073](https://doi.org/10.1086/305073)
- Steidel, C. C., Adelberger, K. L., Shapley, A. E., et al. 2000, ApJ, 532, 170, doi: [10.1086/308568](https://doi.org/10.1086/308568)
- Stevens, J. A., Ivison, R. J., Dunlop, J. S., et al. 2003, Nature, 425, 264, <https://arxiv.org/abs/astro-ph/0309495>
- Strandet, M. L., Weiss, A., De Breuck, C., et al. 2017, ApJL, 842, L15, doi: [10.3847/2041-8213/aa74b0](https://doi.org/10.3847/2041-8213/aa74b0)
- Sun, F., Egami, E., Rawle, T. D., et al. 2021, ApJ, 908, 192, doi: [10.3847/1538-4357/abd6e4](https://doi.org/10.3847/1538-4357/abd6e4)
- Swinbank, A. M., Simpson, J. M., Smail, I., et al. 2014, MNRAS, 438, 1267, doi: [10.1093/mnras/stt2273](https://doi.org/10.1093/mnras/stt2273)
- Tamura, Y., Kohno, K., Nakanishi, K., et al. 2009, Nature, 459, 61, doi: [10.1038/nature07947](https://doi.org/10.1038/nature07947)
- Topping, M. W., Shapley, A. E., Steidel, C. C., Naoz, S., & Primack, J. R. 2018, ApJ, 852, 134, doi: [10.3847/1538-4357/aa9f0f](https://doi.org/10.3847/1538-4357/aa9f0f)
- U, V., Sanders, D. B., Mazzarella, J. M., et al. 2012, ApJS, 203, 9, doi: [10.1088/0067-0049/203/1/9](https://doi.org/10.1088/0067-0049/203/1/9)
- Uchimoto, Y. K., Yamada, T., Kajisawa, M., et al. 2012, ApJ, 750, 116, doi: [10.1088/0004-637X/750/2/116](https://doi.org/10.1088/0004-637X/750/2/116)
- Umehata, H., Tamura, Y., Kohno, K., et al. 2014, MNRAS, 440, 3462, doi: [10.1093/mnras/stu447](https://doi.org/10.1093/mnras/stu447)
- . 2015, ApJL, 815, L8, doi: [10.1088/2041-8205/815/1/L8](https://doi.org/10.1088/2041-8205/815/1/L8)
- . 2017, ApJ, 835, 98, doi: [10.3847/1538-4357/835/1/98](https://doi.org/10.3847/1538-4357/835/1/98)
- Umehata, H., Hatsukade, B., Smail, I., et al. 2018, PASJ, 70, 65, doi: [10.1093/pasj/psy065](https://doi.org/10.1093/pasj/psy065)
- Umehata, H., Fumagalli, M., Smail, I., et al. 2019, Science, 366, 97, doi: [10.1126/science.aaw5949](https://doi.org/10.1126/science.aaw5949)
- van der Walt, S., Colbert, S. C., & Varoquaux, G. 2011, Computing in Science Engineering, 13, 22, doi: [10.1109/MCSE.2011.37](https://doi.org/10.1109/MCSE.2011.37)
- Virtanen, P., Gommers, R., Oliphant, T. E., et al. 2020, Nature Methods, 17, 261, doi: [10.1038/s41592-019-0686-2](https://doi.org/10.1038/s41592-019-0686-2)

- Wardlow, J. L., Smail, I., Coppin, K. E. K., et al. 2011, MNRAS, 415, 1479, doi: [10.1111/j.1365-2966.2011.18795.x](https://doi.org/10.1111/j.1365-2966.2011.18795.x)
- Wes McKinney. 2010, in Proceedings of the 9th Python in Science Conference, ed. Stéfan van der Walt & Jarrod Millman, 56 – 61, doi: [10.25080/Majora-92bf1922-00a](https://doi.org/10.25080/Majora-92bf1922-00a)
- Williams, C. C., Labbe, I., Spilker, J., et al. 2019, ApJ, 884, 154, doi: [10.3847/1538-4357/ab44aa](https://doi.org/10.3847/1538-4357/ab44aa)
- Wilson, G. W., Austermann, J. E., Perera, T. A., et al. 2008, MNRAS, 386, 807, doi: [10.1111/j.1365-2966.2008.12980.x](https://doi.org/10.1111/j.1365-2966.2008.12980.x)
- Yamada, T., Nakamura, Y., Matsuda, Y., et al. 2012, AJ, 143, 79, doi: [10.1088/0004-6256/143/4/79](https://doi.org/10.1088/0004-6256/143/4/79)
- Zavala, J. A., Casey, C. M., da Cunha, E., et al. 2018a, ApJ, 869, 71, doi: [10.3847/1538-4357/aaecd2](https://doi.org/10.3847/1538-4357/aaecd2)
- Zavala, J. A., Montaña, A., Hughes, D. H., et al. 2018b, Nature Astronomy, 2, 56, doi: [10.1038/s41550-017-0297-8](https://doi.org/10.1038/s41550-017-0297-8)
- Zavala, J. A., Casey, C. M., Manning, S. M., et al. 2021, ApJ, 909, 165, doi: [10.3847/1538-4357/abdb27](https://doi.org/10.3847/1538-4357/abdb27)